1991

Measurement of the n=2 Lamb shift in He+ by the anisotropy method

A. Van Wijngaarden

J. Kwela

Gordon W. F. Drake
University of Windsor

PHYSICAL REVIEW A VOLUME 43, NUMBER 7 1 APRIL 1991

Measurement of the $n=2$ Lamb shift in He^+ by the anisotropy method

A. van Wijngaarden, J. Kwela,* and G. W. F. Drake
Department of Physics, University of Windsor, Windsor, Ontario, Canada N9B 3P4
(Received 11 December 1990)

A high-precision measurement of the $2s\,^2S_{1/2}-2p\,^2P_{1/2}$ Lamb shift in He^+ by the quenching-anisotropy method is reported. The theory and experimental method are described in detail. The measured value of 14042.52±0.16 MHz (±11 parts per million) rivals the accuracy of Lamb-shift measurements in hydrogen by microwave resonance. By subtracting the known low-order terms in the Lamb shift, we interpret the results as a measurement of the order $\alpha(Z\alpha)^6mc^2$ and higher contributions to the electron self-energy $G_{SE}(Z\alpha)$. The various contributions to the Lamb shift are discussed, and a revised value for $G_{SE}(Z\alpha)$ at low Z is extracted from high-Z calculations. The theoretical value for the Lamb shift is 14042.51±0.2 MHz, in excellent agreement with experiment. The results provide the most sensitive available determination of $G_{SE}(Z\alpha)$ for low Z. Measurements and calculations for hydrogen and other members of the isoelectronic sequence are discussed.

I. INTRODUCTION

This paper presents the results of an extended series of measurements of the $2s\,^2S_{1/2}-2p\,^2P_{1/2}$ Lamb shift in He^+ by the anisotropy method. Since the method was originally proposed in 1973,[1] successive measurements[2–4] have progressively improved the precision to ±25 parts per million (ppm). The present work obtains a further improvement to ±12 ppm. Combining with previous measurements gives an overall precision of ±11 ppm.

The Lamb shift remains one of the important tests of quantum electrodynamics (QED) in the presence of Coulomb fields. A main motivation for the present work is to test the calculated corrections to the Lamb shift of relative order α^2Z^2 and higher, where α is the fine-structure constant and Z the nuclear charge. For low Z, the Lamb shift $\mathcal{L}$ can be expanded in powers of α and αZ in the form (see, e.g., Ref. 5 and earlier references therein)

$$\mathcal{L}=\frac{8\alpha(Z\alpha)^4mc^2}{6\pi n^3}\{A_{40}+A_{41}\ln(Z\alpha)^{-2}+A_{50}Z\alpha+(Z\alpha)^2[A_{62}\ln^2(Z\alpha)^{-2}+A_{61}\ln(Z\alpha)^{-2}+\Delta G(Z\alpha)] +(\alpha/\pi)[B_{40}+O(Z\alpha)]+O(\alpha^2/\pi^2)\}+\cdots\ , \tag{1}$$

where the ellipsis represents finite-nuclear-mass and -size corrections. Each of the constants A_{ij} can be written as the sum of electron self-energy, vacuum polarization, and anomalous magnetic moment contributions. With the exception of the Bethe logarithm in the self-energy part

$$A_{40}^{SE}=\ln(Z^2R_\infty/k_{nl})+\tfrac{11}{24}\delta_{l,0} \tag{2}$$

all are known analytically in closed form and are well established. For the Bethe logarithm, highly accurate numerical values are available.[6,7] The principal theoretical source of uncertainty comes from the term $\Delta G(Z\alpha)$, which represents the residual contribution from the sum of all higher-order terms in $Z\alpha$ arising from a $Z\alpha$ expansion of the electron self-energy. (There is also a small vacuum polarization contribution.) Mohr's[8] calculation effectively sums the $Z\alpha$ series to infinity, and then subtracts the leading terms shown in Eq. (1) to obtain the residual part $\Delta G(Z\alpha)$. However, the calculation involves multidimensional numerical integrations which limit the accuracy. Since $(Z\alpha)^2$ is four times bigger for He^+ $(Z=2)$ than for H $(Z=1)$, our ±12 ppm measurement in He^+ is equivalent to a ±3 ppm measurement in H for the same sensitivity to the $\Delta G(Z\alpha)$ term. This is substantially better than the currently best ±9 ppm microwave resonance measurement[9] in H. In addition, He^+ is relatively less affected by uncertainties due to uncalculated recoil corrections (see Sec. VI), and to nuclear size corrections. The best existing microwave resonance measurement in He^+ has an accuracy of ±86 ppm.[10]

The anisotropy method used in the present work is based on the principle that when a metastable He^+ $(2s_{1/2})$ ion is quenched to the ground state by the application of a static electric field, the emitted Ly-α radiation is not isotropic, but possesses an anisotropy which is approximately proportional to the Lamb shift. The anisotropy defined by

$$R=(I_\parallel-I_\perp)/(I_\parallel+I_\perp)\ , \tag{3}$$

where $I_\parallel$ and $I_\perp$ are the Ly-α intensities emitted into equal solid angles parallel and perpendicular to the electric field direction, is about 10% for all low-Z hydrogenic ions. In general R is approximately equal to $-3\mathcal{L}/(2\mathcal{F})$, where $\mathcal{L}$ is the Lamb shift and $\mathcal{F}$ is related to the fine-structure splitting by

$$\mathcal{F}=\mathcal{L}-[E(2p_{3/2})-E(2p_{1/2})]\ . \tag{4}$$

The additional energy difference $E(2p_{3/2})-E(2p_{1/2})$ contained in $\mathcal{F}$ is to lowest order a non-QED effect which can be accurately calculated. The anisotropy method is complementary to direct resonance methods in that it measures total intensities integrated over the resonance profile. An important advantage is that the accuracy of the anisotropy method is not limited by the large width Γ of the Lamb shift resonance relative to the shift itself ($\Gamma \simeq \mathcal{L}/10$). The main disadvantage is that one must make high-precision measurements of the relative intensities. This problem is discussed in detail in Sec. III C.

The paper is organized as follows. Section II provides an overview of the quenching theory used to interpret the measured anisotropy in terms of the Lamb shift, including a number of small corrections required for a high-precision measurement. Section III gives a general description of the experimental method, together with considerations relating to various systematic corrections, while Sec. IV describes some specific experimental techniques designed to eliminate signal spikes and measure the anisotropy independent of detector sensitivity. The experimental results are presented in Sec. V, together with the values for the systematic corrections. The various contributions to the Lamb shift are discussed in Sec. VI, and the results interpreted in terms of $G(Z\alpha)$. An important part of the interpretation is a revised determination of $G(Z\alpha)$ at low Z from calculations at high Z discussed in the Appendix. The revised value gives noticeably better agreement with experiment.

II. QUENCHING ANISOTROPY THEORY

An account of the theory of quenching radiation asymmetries in hydrogenic ions has been given by Drake.[11] Here we discuss the main points used to relate the measured anisotropy to the Lamb shift, including some new analytic results for the finite field corrections.

The aim of the theory is to describe the asymmetries in the quenching radiation from the $2s_{1/2}$ state in the presence of a constant electric field in terms of the radiative transition amplitudes and energy separations of the states involved. For atoms or ions such as H and He^+ in fields up to several kV/cm, the dominant field-induced mixing is among the manifold of states $2s_{1/2}$, $2p_{1/2}$, and $2p_{3/2}$. A small correction due to mixing with higher n states and final-state perturbations will be added at the end. Since $^4He^+$ has zero nuclear spin, there is no additional hyperfine structure. In addition, a perturbation expansion in terms of the external electric field strength F is useful provided that the quadratic Stark shifts are much less than the Lamb shift. This corresponds to the condition[12]

$$12(eFa_0/\mathcal{L})^2 \ll 1 \tag{5}$$

where a_0 is the Bohr radius, or $F^2 \ll (6.336\ \text{kV/cm})^2$.

The formalism we use for describing the electric field quenching of the $2s_{1/2}$ state in a static electric field is based on the phenomenological Bethe-Lamb[13] quenching theory, which is in turn derived from the Wigner-Weisskopf[14] analysis for time-dependent perturbations. In this approach, the time-dependent Schrödinger equation is written in a finite basis set of strongly interacting states in the form

$$i\hbar\frac{d\mathbf{a}}{dt}=\underline{H}(t)\mathbf{a}\ , \tag{6}$$

$$\underline{H}(t)=\underline{E}+F(t)\underline{V}\ , \tag{7}$$

where $\mathbf{a}$ is a column vector of state amplitudes, $\underline{E}$ is the diagonal matrix of field-free eigenvalues, $\underline{V}$ is the interaction matrix with the external field, and $F(t)$ describes its time dependence. The key element of phenomenological quenching theory is to replace the field-free eigenvalues E_j by $E_j-i\Gamma_j/2$, where the Γ_j are the field-free level widths. ($\Gamma_j=\gamma_j/2\pi$, where γ_j is the decay rate.) Kelsey and Macek[15] and Hillery and Mohr[16] have shown from quantum electrodynamics that this procedure is justified at least up to terms of relative order α/π. The introduction of level widths has only a small (493 ppm) effect on the final results.

The general solutions to (6) show complex decay patterns and interference effects.[11] However, if the external electric field is switched on adiabatically, the perturbed $2s_{1/2}$ initial state is a stationary state of the form

$$\begin{aligned}\psi(2s_{1/2},m)=a(F)\psi_0(2s_{1/2},m)&\\ +\sum_{m'}[b^{(1/2)}_{m,m'}\psi_0(2p_{1/2},m')&\\ +b^{(3/2)}_{m,m'}\psi_0(2p_{3/2},m')]&\ ,\end{aligned} \tag{8}$$

where ψ_0 denotes the field-free wave functions for the strongly interacting states and the matrices $\underline{b}^{(j)}(j=\frac{1}{2},\frac{3}{2})$ are given by

$$\underline{b}^{(1/2)}=b_{1/2}(F)\boldsymbol{\sigma}\cdot\hat{\mathbf{E}} \tag{9}$$

$$\underline{b}^{(3/2)}=b_{3/2}(F)\begin{bmatrix}-\sqrt{3}\hat{E}_{-1} & \sqrt{2}\hat{E}_0 & -\hat{E}_1 & 0\\ 0 & -\hat{E}_{-1} & \sqrt{2}\hat{E}_0 & -\sqrt{3}\hat{E}_1\end{bmatrix}. \tag{10}$$

The components of $\boldsymbol{\sigma}$ in Eq. (9) are the Pauli spin matrices and the $\hat{E}_q$ ($q=0,\pm1$) are the irreducible tensor components of the unit vector $\hat{E}$ in the electric field direction defined by

$$\hat{E}_{\pm1}=\mp\frac{1}{\sqrt{2}}(\hat{E}_x\pm i\hat{E}_y),\quad \hat{E}_0=\hat{E}_z\ .$$

Direct numerical integrations of the full time-dependent Eq. (6) for our field geometry show that the adiabatic condition is well satisfied.[17]

Since the energies of the $2s_{1/2}$ ($m=\pm\frac{1}{2}$) states remain degenerate in an electric field and are independent of the field orientation, the forms of Eqs. (9) and (10) remain valid to all orders of perturbation theory. The only explicit dependence on field strength is through the three overall multiplying factors $a(F)$, $b_{1/2}(F)$, and $b_{3/2}(F)$. To lowest order in F, they are given by

$$a(F)=1+O(F^2)\ , \tag{11}$$

$$b_{1/2}(F)=\frac{eF\langle 2p_{1/2}\|r\|2s_{1/2}\rangle}{\sqrt{6}(\mathcal{L}+i\Gamma/2)}+O(F^3)\ , \tag{12}$$

$$b_{3/2}(F)=\frac{eF\langle 2p_{3/2}\|r\|2s_{1/2}\rangle}{\sqrt{12}(\mathcal{J}+i\Gamma/2)}+O(F^3)\ , \tag{13}$$

where Γ is the level width of the $2p$ state, and the reduced dipole matrix elements, including lowest order relativistic corrections, are summarized in Table I. Higher-order perturbation corrections to the above equations can readily be calculated analytically.[12] Alternatively, the coefficients $a(F)$, $b_{1/2}(F)$, $b_{3/2}(F)$ are the eigenvector components obtained from an exact diagonalization of the Hamiltonian matrix in the $2s_{1/2},2p_{1/2},2p_{3/2}$ basis set of strongly interacting states.

The properties of the quenching radiation are determined by the 2×2 matrix $\underline{A}$ with elements

$$A_{m,m'}=\langle \psi_0(1s_{1/2},m)|\boldsymbol{\alpha}\cdot\hat{\mathbf{e}}e^{-i\mathbf{k}\cdot\mathbf{r}}|\psi(2s_{1/2},m')\rangle\ , \tag{14}$$

where $\hat{\mathbf{e}}$ is the polarization vector of the emitted radiation, $\mathbf{k}$ is the wave vector ($|\mathbf{k}|=\omega/c$), $\boldsymbol{\alpha}$ is the 4×4 Dirac matrix and $\psi(2s_{1/2},m')$ is the perturbed initial state given in terms of the field-free states by Eq. (8). The evaluation of the matrix elements in (14) is facilitated by the partial-wave expansion of the plane wave in (14). Keeping only the electric dipole ($E1$), magnetic dipole ($M1$), and magnetic quadrupole ($M2$) terms, the result is[18]

$$\hat{\mathbf{e}}e^{-i\mathbf{k}\cdot\mathbf{r}}=(\tfrac{3}{8}\pi)^{1/2}\sum_M\{e_M\mathbf{a}_{1,M}^{(1)*}+i(\hat{\mathbf{k}}\times\hat{\mathbf{e}})_M\mathbf{a}_{1,M}^{(0)*}+i(\tfrac{10}{3})^{1/2}[\hat{\mathbf{k}},\hat{\mathbf{k}}\times\hat{\mathbf{e}}]_{2,M}\mathbf{a}_{2,M}^{(0)*}\}\ . \tag{15}$$

The notation $[\mathbf{a},\mathbf{b}]_{2,M}$ denotes the vector-coupled product

$$[\mathbf{a},\mathbf{b}]_{2,M}=\sum_{m,m'}\langle 1m1m'|2M\rangle a_m b_{m'} \tag{16}$$

and the $\mathbf{a}_{L,M}^{(\lambda)}$ are the standard operators for electric and magnetic multipole transitions given by (in the Coulomb gauge)

$$\mathbf{a}_{L,M}^{(1)}=\left[\frac{L}{2L+1}\right]^{1/2}g_{L+1}(kr)\mathbf{Y}_{LL+1M}+\left[\frac{L+1}{2L+1}\right]^{1/2}g_{L-1}(kr)\mathbf{Y}_{LL-1M} \tag{17}$$

for electric multipoles and

$$\mathbf{a}_{L,M}^{(0)}=g_L(kr)\mathbf{Y}_{LLM} \tag{18}$$

for magnetic multipoles. The $\mathbf{Y}_{LJM}$ are vector spherical harmonics as defined by Edmonds,[19] and the radial functions $g_L(kr)$ are related to spherical Bessel functions by

$$g_L(kr)=4\pi i^L j_L(kr)\ . \tag{19}$$

Using the Wigner-Eckart theorem, the transition matrix $\underline{A}$ defined by (14) can then be written in the form

$$\underline{A}=V_0\hat{\mathbf{e}}\cdot\hat{E}\mathbb{1}+\boldsymbol{\sigma}\cdot[iV_1(\hat{\mathbf{e}}\times\hat{\mathbf{E}})+M(\hat{\mathbf{k}}\times\hat{\mathbf{e}})]\ , \tag{20}$$

where

$$V_0=V_{1/2}+2V_{3/2}\ ,$$
$$V_1=V_{1/2}-V_{3/2}+M_{3/2}\ ,$$
$$M=M_{1/2}+2i(\hat{\mathbf{k}}\cdot\hat{\mathbf{e}})M_{3/2}\ , \tag{21}$$

and

$$V_{1/2}=-\frac{b_{1/2}(F)}{4\pi^{1/2}}\langle 1s_{1/2}\|\boldsymbol{\alpha}\cdot\mathbf{a}_1^{(1)*}\|2p_{1/2}\rangle\ , \tag{22}$$

TABLE I. Summary of transition matrix elements.

Matrix element	Value
$\langle 2p_{1/2}\|\mathbf{r}\|2s_{1/2}\rangle$	$3\sqrt{2}a_0Z^{-1}(1-\frac{5}{12}\alpha^2Z^2)$
$\langle 2p_{3/2}\|\mathbf{r}\|2s_{1/2}\rangle$	$-6a_0Z^{-1}(1-\frac{1}{6}\alpha^2Z^2)$
$\langle 1s_{1/2}\|\boldsymbol{\alpha}\cdot\mathbf{a}_1^{(1)*}\|2p_{1/2}\rangle$	$\frac{ika_0}{Z}\left[\frac{2\pi}{3}\right]^{1/2}\frac{2^9}{3^5}\left[1-\left[\frac{11}{96}+\frac{3}{2}\ln 2-\ln 3\right]\alpha^2Z^2\right]$
$\langle 1s_{1/2}\|\boldsymbol{\alpha}\cdot\mathbf{a}_1^{(1)*}\|2p_{3/2}\rangle$	$-\frac{ika_0}{Z}\left[\frac{4\pi}{3}\right]^{1/2}\frac{2^9}{3^5}\left[1-\left[\frac{11}{48}+\frac{5}{4}\ln 2-\frac{3}{4}\ln 3\right]\alpha^2Z^2\right]$
$\langle 1s_{1/2}\|\boldsymbol{\alpha}\cdot\mathbf{a}_1^{(0)*}\|2s_{1/2}\rangle$	$ka_0Z^2\alpha^3(4\pi)^{1/2}\frac{2^4}{3^4}\left[1+0.4193\alpha^2Z^2\right]$
$\langle 1s_{1/2}\|\boldsymbol{\alpha}\cdot a_2^{(0)*}\|2p_{3/2}\rangle$	$i(ka_0)^2\alpha\pi^{1/2}Z^{-1}\frac{2^8}{3^5}\left[1-0.1821\alpha^2Z^2\right]$
$\langle 2p_{1/2}\|z\|2s_{1/2}\rangle$	$\sqrt{3}a_0Z^{-1}(1-\frac{5}{12}\alpha^2Z^2)$
$\langle 2p_{3/2}\|z\|2s_{1/2}\rangle$	$-\sqrt{6}a_0Z^{-1}(1-\frac{1}{6}\alpha^2Z^2)$
$\langle 1s\|z\|2p\rangle$	$2^7\sqrt{2}a_0Z^{-1}/3^5$
$\langle 2p\|z\|2s\rangle$	$-3a_0Z^{-1}$

$$V_{3/2}=-\frac{b_{3/2}(F)}{4(2\pi)^{1/2}}\langle 1s_{1/2}\|\boldsymbol{\alpha}\cdot\mathbf{a}_1^{(1)*}\|2p_{1/2}\rangle \;, \tag{23}$$

$$M_{1/2}=\frac{ia(F)}{4\pi^{1/2}}\langle 1s_{1/2}\|\boldsymbol{\alpha}\cdot\mathbf{a}_1^{(0)*}\|2s_{1/2}\rangle \;, \tag{24}$$

$$M_{3/2}=-\frac{b_{3/2}(F)}{4(2\pi/3)^{1/2}}\langle 1s_{1/2}\|\boldsymbol{\alpha}\cdot\mathbf{a}_2^{(0)*}\|2p_{3/2}\rangle \;. \tag{25}$$

Values of the above reduced matrix elements are summarized in Table I.

The physical significance of the above terms is as follows. $V_{1/2}$ and $V_{3/2}$ represent the amplitudes for electric field quenching of the $2s_{1/2}$ state via the admixture of the $2p_{1/2}$ and $2p_{3/2}$ intermediate states, respectively, with the emission of an $E1$ photon, while $M_{3/2}$ is a small $M2$ correction. All three of these terms are (approximately) proportional to the electric field strength through the b_j coefficients. The combination V_0 comes from transitions with $\Delta m=0$ in Eq. (14), and the $E1$ part of V_1 comes from transitions with $\Delta m=\pm1$. $M_{1/2}$ is the amplitude for spontaneous relativistic $M1$ transitions.[20] It is to a first approximation independent of field strength.

The electron spin polarization $\mathbf{P}$ of the initial $2s_{1/2}$ state is described in general by the density matrix

$$\underline{\rho}=\tfrac{1}{2}(\underline{1}+\boldsymbol{\sigma}\cdot\mathbf{P}) \;. \tag{26}$$

The emitted radiation is then characterized by the four vectors $\hat{\mathbf{e}}$, $\hat{\mathbf{k}}$, $\hat{\mathbf{E}}$, and $\mathbf{P}$. A detailed expression for the decay rate per unit solid angle, summed over final states and averaged over initial states, is obtained by substituting the above results into

$$w\,d\Omega=\frac{e^2k}{2\pi\hbar}\mathrm{Tr}(\underline{\rho}\underline{A}^\dagger\underline{A})d\Omega \tag{27}$$

where Tr denotes the trace. The general result for arbitrary $\hat{\mathbf{e}}$, $\hat{\mathbf{k}}$, $\hat{\mathbf{E}}$, and $\mathbf{P}$ has been given previously.[18] For the present experiment, the $2s_{1/2}$ state is unpolarized and the detectors are not sensitive to the polarization $\hat{\mathbf{e}}$ of the emitted radiation. Setting $\mathbf{P}=0$ and summing (27) over two orthogonal vectors $\hat{\mathbf{e}}$ perpendicular to $\hat{\mathbf{k}}$ yields

$$w(\hat{\mathbf{k}})d\Omega=\frac{e^2k}{\pi\hbar}I(\hat{\mathbf{k}})d\Omega$$

with

$$I(\hat{\mathbf{k}})=\tfrac{1}{2}|V_0|^2[1-(\hat{\mathbf{k}}\cdot\hat{\mathbf{E}})^2]+\tfrac{1}{2}|V_1|^2[1+(\hat{\mathbf{k}}\cdot\hat{\mathbf{E}})^2] +|M|^2+2\,\mathrm{Im}(M^*V_1)(\hat{\mathbf{k}}\cdot\hat{\mathbf{E}}) \;. \tag{28}$$

The relative intensities in the directions parallel and perpendicular to the quenching field are then obtained by setting $\hat{\mathbf{k}}\cdot\hat{\mathbf{E}}=1$ and $\hat{\mathbf{k}}\cdot\hat{\mathbf{E}}=0$, respectively. The last term, which is linear in $\hat{\mathbf{k}}\cdot\hat{\mathbf{E}}$, does not contribute because each signal measurement is averaged over the directions $\mathbf{k}$ and $-\hat{\mathbf{k}}$. The $|M|^2$ term is small enough at our quenching fields to be omitted altogether.

Equation (28) is in a form convenient for calculating the anisotropy. However, the significance of the terms can be more easily seen by substituting Eqs. (21) and regrouping the terms in the form

$$I(\theta)=|V_{1/2}|^2+2|V_{3/2}|^2+|M_{1/2}|^2+\tfrac{2}{3}|M_{3/2}|^2+2\,\mathrm{Im}[M_{1/2}^*(V_{1/2}-V_{3/2}-M_{3/2})]P_1(\cos\theta) -\{|V_{3/2}|^2-\tfrac{1}{3}|M_{3/2}|^2+2\,\mathrm{Re}[V_{1/2}^*V_{3/2}+M_{3/2}^*(V_{1/2}-V_{3/2})]\}P_2(\cos\theta) \;, \tag{29}$$

where the $P_L(\cos\theta)$ are Legendre polynomials and $\cos\theta=\hat{\mathbf{k}}\cdot\hat{\mathbf{E}}$. The above clearly shows that all cross terms vanish on integrating over angles, leaving only a sum of absolute squares for the various radiative decay channels which contribute to the total quench rate. The anisotropy comes predominantly from the $\mathrm{Re}(V_{1/2}^*V_{3/2})$ interference term between the $2p_{1/2}$ and $2p_{3/2}$ intermediate states.

For purposes of presenting the results, we first consider the limit of weak fields and nonrelativistic matrix elements. In this limit, the ratio

$$\rho=V_{3/2}/V_{1/2} \tag{30}$$

is approximately the ratio of energy denominators given by

$$\rho_0=\frac{\mathcal{L}+i\Gamma/2}{\mathcal{F}+i\Gamma/2} \tag{31}$$

and to the same approximation, $I(\theta)$ reduces to

$$I_0(\theta)=|V_{1/2}|^2[1+\mathrm{Re}(\rho_0)(1-3\cos^2\theta) +\tfrac{1}{2}|\rho_0|^2(5-3\cos^2\theta)] \tag{32}$$

and the anisotropy R, defined by Eq. (3), becomes

$$R_0=-\frac{[3\,\mathrm{Re}(\rho_0)+\frac{3}{2}|\rho_0|^2]}{[2-\mathrm{Re}(\rho_0)+\frac{7}{2}|\rho_0|^2]} \;. \tag{33}$$

This lowest-order result emphasizes that the anisotropy is determined primarily by the ratio $\mathcal{L}/\mathcal{F}\simeq-0.08$ for all low-Z ions, and so $R_0\simeq0.1$ over a wide range of nuclear charge.

There are several small corrections to the above result which must be taken into account in the analysis of high-precision measurements. We now consider each of them in turn.

Finite electric field effects introduce higher-order perturbation corrections to the mixing coefficients $a(F)$, $b_{1/2}(F)$, and $b_{3/2}(F)$ which appear in Eqs. (22)–(25). A simple recursion relation is given by Drake[12] for calculating the perturbation expansion to arbitrary order. Since ρ is a ratio independent of wave-function normalization, the general results can be simplified by choosing the normalization so that $a(F)=1$. [This corresponds to the intermediate normalization $\langle\psi_0(2s_{1/2})|\psi(2s_{1/2})\rangle=1$.] The expansion of the $b_j(F)$ is then of the form

$$b_j(F)=b_j^{(1)}(F)[1+(eF)^2W_j^{(2)}+(eF)^4W_j^{(4)}+\cdots] , \tag{34}$$

where the $b_j^{(1)}(F)$ $(j=\frac{1}{2},\frac{3}{2})$ are the first-order values given by (12) and (13), and the $W_j^{(n)}$ are given by

$$W_j^{(2)}=-E_2/\Delta_j , \tag{35}$$

$$W_j^{(4)}=(E_2/\Delta_j)^2-E_4/\Delta_j , \tag{36}$$

with $\Delta_{1/2}=\mathcal{L}+i\Gamma/2$, $\Delta_{3/2}=\mathcal{F}+i\Gamma/2$, and E_2 and E_4 are the second- and fourth-order perturbation energy coefficients for the Stark shift of the $2s_{1/2}$ state. Defining

$$T_p=\sum_{j=1/2}^{3/2}|\langle 2s_{1/2}|z|2p_j\rangle|^2/(\Delta_j)^p , \tag{37}$$

they are $E_2=T_1$ and $E_4=-T_1T_2$. Then, corresponding to the expansions of the $b_j(F)$, there are similar expansions for ρ and R_0 of the forms

$$\rho=\rho_0+F^2\rho_2+F^4\rho_4+\cdots \tag{38}$$

and

$$R=R_0+F^2R_2+F^4R_4+\cdots . \tag{39}$$

After considerable algebra, the coefficients reduce to

$$\rho_2=3\left[\frac{ea_0}{Z\Delta_{1/2}}\right]^2\rho_0(1+2\rho_0)(1-\rho_0) , \tag{40}$$

$$\rho_4=-3\left[\frac{ea_0}{Z\Delta_{1/2}}\right]^2\rho_2(1+\rho_0+4\rho_0^2) , \tag{41}$$

$$R_2=-2\left[\frac{Z}{ea_0D_0}\right]^2|\rho_2|^2\mathrm{Re}(\Delta_{1/2}\Delta_{3/2}) , \tag{42}$$

$$R_4=-2\left[\frac{Z}{ea_0D_0}\right]^2\mathrm{Re}(\rho_4^*\rho_2\Delta_{1/2}\Delta_{3/2}) -3|\rho_2|^2[1-4\,\mathrm{Re}(\rho_0)]/D_0^2 +R_2\mathrm{Re}[\rho_2(1-7\rho_0^*)]/D_0 , \tag{43}$$

where

$$D_0=2-\mathrm{Re}(\rho_0)+\tfrac{7}{2}|\rho_0|^2$$

is the denominator of Eq. (33). Using the input data in Table II, the numerical values are $R_2=5.8471\times10^{-4}$ $(\mathrm{kV/cm})^{-2}$ and $R_4=-3.8084\times10^{-6}$ $(\mathrm{kV/cm})^{-4}$. Terms beyond R_4 do not make a significant contribution of field strengths less than 1 kV/cm.

The mixing of the $2s_{1/2}$ state with higher-lying np states and perturbations to the $1s_{1/2}$ final state are adequately treated as an additional first-order electric dipole perturbation. Since the fine structure of the np states becomes negligible relative to the much larger $2s$-np and $1s$-np Coulomb splittings, the effect of these additional intermediate states is to add a small background to the quench radiation which is proportional to $\hat{\mathbf{e}}\cdot\hat{\mathbf{E}}$. The additional states are taken into account by first defining the quantities

$$B=\sum_{n=3}^{\infty}\frac{\langle 1s|z|np\rangle\langle np|z|2s\rangle}{E(2s)-E(np)} , \tag{44}$$

TABLE II. Input data for calculating the He^+ anisotropy.

Quantity	Value
$\mathcal{F}$	175 593.54(3) MHz[a]
γ_{2p}	$1.003\,07\times10^{-10}$ sec^{-1}
$(\delta R/R_0)_n$	-23.7×10^{-6}
$(\delta R/R_0)_{\mathrm{rel}}$	6.4×10^{-6}
$(\delta R/R_0)_{M2}$	-65.4×10^{-6}
R_2	5.8471×10^{-4} $(\mathrm{kV/cm})^{-2}$
R_4	-3.8084×10^{-6} $(\mathrm{kV/cm})^{-4}$
F	631.05 V/cm

[a]Numbers in parentheses indicate the uncertainties in the final figures quoted.

$$C=\sum_{n=2}^{\infty}\frac{\langle 1s|z|np\rangle\langle np|z|2s\rangle}{E(1s)-E(np)} , \tag{45}$$

and then replacing V_0 in Eq. (20) by $V_0-ikeF(B+C)$. Neglecting the level widths, the corresponding correction to R_0 is

$$\left[\frac{\delta R}{R_0}\right]_n=2(B+C)\frac{\mathcal{F}}{\zeta}\left[\frac{1+2\rho_0}{2+\rho}\right](1+R_0) \tag{46}$$

with

$$\zeta=\langle 1s|z|2p\rangle\langle 2p|z|2s\rangle . \tag{47}$$

The values of B and C can be calculated exactly by implicit summation techniques[21] with the results

$$B=-(25)2^9/(3^6\sqrt{2})a_0^3/e^2 ,$$

$$C=(7)2^9/(3^6\sqrt{2})a_0^3/e^2 .$$

Substituting these values, together with the transition matrix elements given in Table I, yields

$$\left[\frac{\delta R}{R_0}\right]_n=\frac{3\mathcal{F}}{\hbar\omega}\left[\frac{1+2\rho_0}{2+\rho_0}\right](1+R_0) , \tag{48}$$

where $\hbar\omega=(3/8)Z^2e^2/a_0$ is the $2s$-$1s$ transition energy. For He^+, the numerical value is -23.7×10^{-6}.

Relativistic corrections to the transition matrix elements can be taken into account through their effect on ρ. Since ρ is defined by Eq. (30), the correction to ρ_0 defined by Eq. (31) due to relativistic effects is

$$\delta\rho/\rho_0=\mu_{3/2}+\mu'_{3/2}-\mu_{1/2}-\mu'_{1/2} , \tag{49}$$

where the μ_j and μ'_j are the fractional corrections of $O(\alpha^2Z^2)$ to the matrix elements $\langle 2p_j\|\mathbf{r}\|2s_{1/2}\rangle$ and $\langle 1s_{1/2}\|\boldsymbol{\alpha}\cdot\mathbf{a}^{(1)*}\|2p_j\rangle$, respectively. The values taken from Table I are

$$\mu_{3/2}=-\tfrac{1}{6}\alpha^2Z^2,\quad \mu_{1/2}=-\tfrac{5}{12}\alpha^2Z^2 ,$$

$$\mu'_{3/2}=(-\tfrac{11}{48}-\tfrac{5}{4}\ln2+\tfrac{3}{4}\ln3)\alpha^2Z^2 ,$$

$$\mu'_{1/2}=(-\tfrac{11}{96}-\tfrac{3}{2}\ln2+\ln3)\alpha^2Z^2 .$$

Substituting into Eq. (33) results in

$$\left[\frac{\delta R}{R_0}\right]_{\text{rel}} = 2(\mu_{3/2}+\mu'_{3/2}-\mu_{1/2}-\mu'_{1/2}) \times \left[\frac{1+2\rho_0}{2+\rho_0}\right]\left[\frac{1+R_0}{1-\rho_0}\right] . \quad (50)$$

For He^+, the numerical value is 6.4×10^{-6}.

The final small correction arises from the $2p_{3/2}$-$1s_{1/2}$ magnetic quadrupole ($M2$) contribution $M_{3/2}$ to Eq. (29). The importance of this term was first pointed out by Hillery and Mohr.[16] Keeping only the term linear in $M_{3/2}$ results in a correction,

$$\Delta I_0(\theta) = \mathrm{Re}[M^*_{3/2}(V_{1/2}-V_{3/2})](1-3\cos^2\theta) , \quad (51)$$

to $I_0(\theta)$ given by Eq. (32). Neglecting the level widths, the corresponding correction to R_0 is

$$\left[\frac{\delta R}{R_0}\right]_{M2} = \frac{M_{3/2}}{V_{3/2}}\frac{(1-\rho_0)(1-R_0/3)}{(1+\rho_0/2)} = -\frac{9\alpha^2 Z^2}{32}\frac{(1-\rho_0)(1-R_0/3)}{(1+\rho_0/2)} . \quad (52)$$

For He^+, the numerical value is -65.4×10^{-6}.

Beyond the above relativistic and $M2$ corrections of $O(\alpha^2 Z^2)$, one should consider QED corrections to the quenching theory of $O(\alpha^3 Z^2)$. As discussed by Lévy,[22] radiative corrections to the transition matrix elements introduce j-independent multiplying factors in the nonrelativistic electric dipole approximation. These cancel when the anisotropy ratio is formed. The largest surviving effect is an anomalous-magnetic-moment correction to the $2s_{1/2}-2p_{3/2}-1s_{1/2}$ $M2$ transition amplitude, which is smaller than Eq. (52) by a factor of $O(\alpha/\pi)$. The terms already considered should therefore be adequate for the analysis of experiments down to accuracies of a few ppm.

In summary, the theoretical value for the anisotropy is

$$R_T = R_0\left[1+\left[\frac{\delta R}{R_0}\right]_n+\left[\frac{\delta R}{R_0}\right]_{\text{rel}}+\left[\frac{\delta R}{R_0}\right]_{M2}\right] + R_2(eF)^2+R_4(eF)^4+O(F^6) + O(\alpha^3 Z^2/\pi)+O(\alpha^4 Z^4) . \quad (53)$$

III. EXPERIMENTAL METHOD

A. Overall plan

Figure 1 shows a schematic diagram of the apparatus used to measure the quenching anisotropy. The overall design has been described before,[3] but the modifications to the detection system mentioned in Ref. 4 require a detailed description. Briefly, the overall plan is as follows. A He^+ ion beam containing about 0.5% metastables is obtained by passing 134.2-keV ground-state He^+ ions through a gas cell. The magnetic lens shown in the diagram improves the final beam current (8 μA) entering the Faraday cup by an order of magnitude. In the quenching cell, the beam is subjected to a static electric field by supplying opposite polarities to two pairs of cylindrical rods mounted on insulators in a quadrupole arrangement. The resulting Ly-α radiation emitted parallel ($I_\parallel$) and perpendicular ($I_\perp$) to the field direction is detected simultaneously by measuring the photoelectric current from the photosensitive cones A, B, C, and D.

Beam contamination by ions other than $He^+(2s)$ and $He^+(1s)$ is kept small by the following strategies. First, the long 900-ns flight time from the exit of the gas cell to the observation region allows the majority of highly-excited-state ions to decay to the ground state. Second, small transverse electric fields are applied in the region

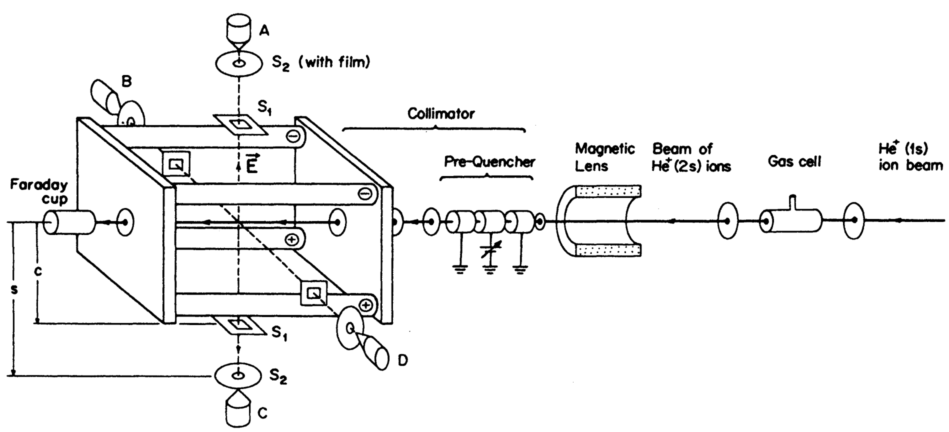

FIG. 1. Schematic diagram of the apparatus for the He^+ anisotropy measurement. The four metal rods in the quenching cell are 1.2700(2) cm in diameter and are supported 4.064(1) cm apart on insulators. The length of the cell is 15.24 cm. S_1 and S_2 are photon collimating slits with $c=7.117(2)$ cm and $s=21.999(3)$ cm.

between the gas cell and the collimator to separate neutral atoms from the ion beam. Third, a small axial electric field of 100 V/cm is maintained between the electrodes of the prequencher (see Fig. 1) to ionize any highly excited states which might survive the long flight path from the gas cell. However, the main purpose of the prequencher is to apply a sufficiently strong electric field to depopulate the $2\,^2S_{1/2}$ state for purposes of noise determination, as described in Sec. IV A.

B. The quenching field and beam deflection

As described above, a transverse electric field is applied to the beam as it traverses the quenching cell. Calling the beam axis the y axis, the field reaches a maximum $F_0=|\mathbf{E}_0|$ at the center $y_0=7.62$ cm of the observation region, as measured from the entrance slit. The field not only quenches the metastable states, but also produces a deflection of the ions in the transverse direction. First-order deflection corrections cancel out because the quenching radiation intensities are simultaneously measured in all four directions, but there remains a small second-order correction. The y dependence of the quenching field must therefore be known to some precision. A previously described method for calculating the field has been devised[17] with the results for $F(y)$ shown in Fig. 2. The field (in V/cm) at the center of the cell is given by

$$F_0=0.8861V/a\ , \tag{54}$$

where $a=2.032$ cm is half the distance between the centers of adjacent rods, each with a diameter of 1.270

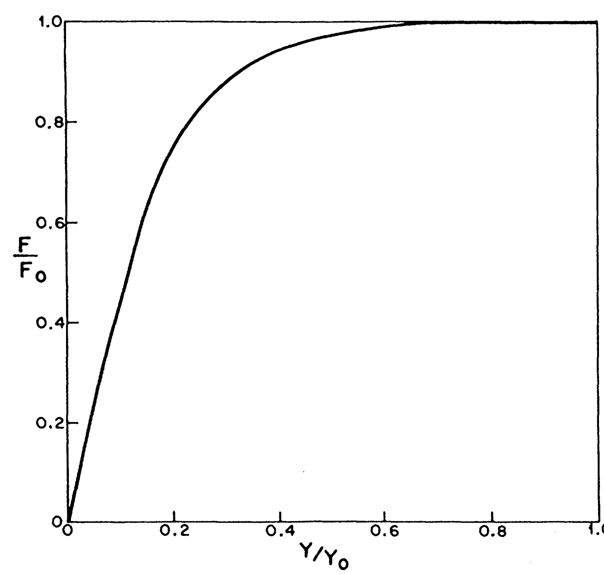

FIG. 2. The y dependence of the electric field strength in the quenching cell along the beam axis. y_0 is the distance from the entrance slit to the center (i.e., one-half of the cell length) and F_0 is the field strength at the center.

cm, and V is the magnitude of the potential in volts for the opposite polarities on two pairs of adjacent rods.

Starting at $y=0$ where the beam enters the cell with velocity v, the transverse velocity $v_z(y)$ in the $\mathbf{E}$ direction is

$$\frac{v_z(y)}{v}=\frac{F_0y_0}{2V_a}\int_0^{y/y_0}\left[\frac{F(y')}{F_0}\right]d\left[\frac{y'}{y_0}\right]\ , \tag{55}$$

where $V_a=134.2$ kV is the accelerating potential for the ion beam, and the transverse deflection is

$$z(y)=y_0\int_0^{y/y_0}\left[\frac{v_z(y')}{v}\right]d\left[\frac{y'}{y_0}\right]\ . \tag{56}$$

As discussed further below, the detection system is somewhat more complicated than shown in Fig. 1 because each slit s_1 actually consists of a pair of rectangular slits mounted in tandem along the beam axis at distances of 1.524 cm on either side of the center y_0. At these locations, the strength of the field is reduced by a factor of 0.997 66 from the central value F_0. The correct quenching field (in V/cm) to be used in Eq. (53) is therefore

$$F=0.884\,03V/a \tag{57}$$

in place of (54). All the data were taken at a single field strength of $F=631.05$ V/cm.

C. Photon detectors

Each of the four detector systems shown in Fig. 1 is actually a pair of identical detectors placed a distance $l=3.048$ cm apart along the ion beam as shown in Fig. 3. The Ly-α photons from the beam pass a collimator consisting of a rectangular entrance slit s_1 and a circular exit slit s_2, and then strike a photosensitive cone P. The cylindrical housing C, kept as a positive potential V_C, collects the photoelectrons and the high-precision electrometer E (Keithley Model 642 LNFA) measures the photocurrent. The photocurrent is independent of V_C in the range 1–200 V studied. The shields Sh prevent photons from crossing between the two collimator systems.

The photoelectric yield of a cone generally improves as its angle becomes sharper. However, in order to ensure that the detector systems respond equally to photons of different polarization, the cone angles were kept large (96°). To compensate for the loss of sensitivity due to the large cone angle, the cones were coated with a layer of MgF_2 of a few hundred Å thickness, thereby enhancing the yield to about 20%. The photon detection systems have been designed to collect as large a photon signal as possible with the requirement that the range of observation directions allowed by the finite sizes of the photon collimation slits is sufficiently small to control systematic errors (see Sec. V B 2). The doubling of the photon detection system as in Fig. 3 allows this limitation on signal strength to be surpassed.

We have introduced the above photon detection system in place of standard photon counting techniques because of nonlinearities which are inherent in photon counting. The problem is that all electron multipliers produce a pulse height distribution which, for high count rates, is weakly count-rate dependent due to variations in the electron multiplication process. For example, in trial runs with photomultipliers, we found deviations from a linear response approaching 500 ppm at count rates of 10^4 counts/sec. In addition, dead time corrections become increasingly troublesome for high count rates. Both problems are avoided by directly collecting and measuring the photoelectron current emitted from a large surface area without further amplification. The disadvantage is that the photoelectron currents produced are small ($\sim 10^{-13}$ A). One must thus take care to ensure that stray electrons and low-energy ions created by collisions of the fast ion beam with the residual gas ($\sim 6\times 10^{-8}$ Torr) are not detected by the cones. We suppressed stray particles by imposing an axial magnetic field of 20.5 G in the observation region to confine the electrons traveling with the beam near its axis, and by covering the exit slits s_2 of the photon collimators with thin (~ 500 Å) aluminum films. Electrons that are ejected from the back surface of the films are suppressed by a repeller plate kept at -300 V.

Each of the detection systems is connected to its own high-precision electrometer, whose analog output in turn is fed to a digital voltmeter (Hewlett Packard Model 3457A). The final output, normalized to the ion beam current, is stored in a computer. In previous experiments,[4] only two electrometers were available for the four

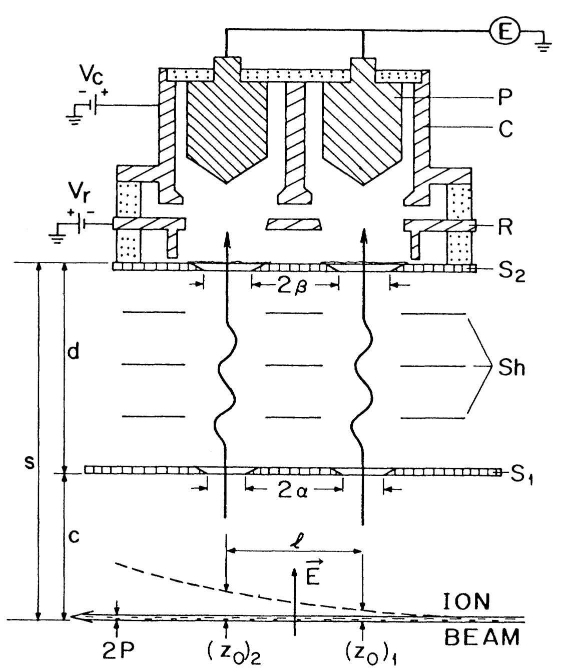

FIG. 3. Details of the photon detection systems A, B, C, and D shown in Fig. 1. The beam diameter ($2p$) is 0.228 cm, the width 2α of the rectangular slit S_1 is 1.245 cm, the diameter 2β of the circular slit S_2 is 1.270 cm, and the cone angles are 96°. The beam deflections $(z_0)_1$ and $(z_0)_2$ [see Eq. (65)] due to the transverse quenching field are exaggerated for clarity.

detectors, which required the connection of two opposite pairs of detectors via a long cable. The elimination of these cables and their associated electronic noise has significantly improved the overall stability of the present measurements. The signal-to-noise ratio for each of the detection systems now is about 1000.

D. Detector linearity

The accuracy of an anisotropy measurement is ultimately limited by the *linearity* (as opposed to absolute accuracy) of the photon-detection system. It is therefore necessary to verify that the degree of linearity for the current measurements is sufficiently high to measure the anisotropy to a precision of the part per million level.

One potential source of nonlinearity is the finite voltage coefficient of the resistance in the input stage of the electrometer, where the photoelectron current is converted into a voltage signal. To minimize this voltage effect, the input resistor of 10^{12} Ω was constructed by connecting four high-quality resistors in series so that for typical currents of 10^{-13} A, the potential across a component resistor is at most 50 mV. This ensures[23] that the linearity between the current and its voltage analog at the input state is well within 1 ppm.

Another potential problem is the nonlinearity between the output voltage and the input voltage over the range 100–200 mV used in the experiment. For this range, the linearity must be better than 10 μV per volt input. This is less stringent than the 5 μV per volt linearity of the Keithley Model 642 electrometers.

It is the high degree of linearity of our photon-detection systems at high-photon fluxes that has allowed a dramatic improvement over our earlier results obtained by photon counting techniques.[2]

IV. MEASUREMENT TECHNIQUES

A. Photoelectron current

To eliminate effects from ion beam current fluctuations, the photoelectron current for each detector pair is normalized to the beam current and time averaged for 30 sec. The normalized photoelectron currents are quite stable. However, superimposed are occasional current spikes originating from α particles and cosmic rays, as well as more gentle fluctuations induced by earthquakes. The magnitude of these fluctuations are typically a factor of 10 smaller than the signal. Similar variations of course also occur during noise measurements, which we define as the quenching signal that still persists when the $2\,{}^2S_{1/2}$ ions are removed from the beam by prequenching. Since both the signal and noise current suffer from similiar extraneous fluctuations, the final time-averaged signal with the noise subtracted is not affected on average. However, as shown in Sec. V A, the precision is significantly improved when the current spikes are removed.

B. Anisotropy

The quantity directly measured is the intensity ratio $r = I_{\parallel}/I_{\perp}$, which is related to the anisotropy R by

$$R=\frac{r-1}{r+1} . \tag{58}$$

The need to measure the relative sensitivities of the detectors, which would otherwise severely limit the accuracy, can be avoided by measuring r for all possible 90° rotations of the electric field in Fig. 1. The field can readily be rotated by simply switching the polarities on the quadrupole rods in a cyclic manner. As a particular example, let θ be the angle between $\mathbf{E}$ and the CA axis. Then, for any pair of adjacent detectors, say A and B, four current ratios

$$r(0)=A(0)/B(0), \quad r(\pi/2)=B(\pi/2)/A(\pi/2) ,$$

$$r(\pi)=A(\pi)/B(\pi), \quad r(3\pi/2)=B(3\pi/2)/A(3\pi/2)$$

can be obtained, where $A(\theta)$ and $B(\theta)$ are the simultaneously measured and time-averaged photoelectron currents. Then the combination

$$r_{AB}=\tfrac{1}{2}\{[r(0)r(\pi/2)]^{1/2}+[r(\pi)r(3\pi/2)]^{1/2}\} \tag{59}$$

is independent of the sensitivities. Furthermore, the average

$$r=\tfrac{1}{4}(r_{AB}+r_{BC}+r_{CD}+r_{DA}) \tag{60}$$

over all four adjacent detector pairs does not contain a first-order correction due to transverse beam deflections (beam bending) in the quenching field. Small second-order corrections for this and other systematic effects are discussed in Sec. V B.

A residual dependence on detector sensitivity arises from the use of the detector pairs mounted in tandem along the beam axis because the beam bending correction is larger downstream than it is upstream. A correction for this was avoided by averaging over two sets of observations with the upstream and downstream detectors interchanged. A 30% difference is known to exist between the two sets of detectors due to variations in thickness of the Al films covering the entrance slits.

V. RESULTS

A. The uncorrected data

We will denote the two sets of measurements before and after interchanging the upstream and downstream detectors by the labels I and II. Set I corresponds to the higher sensitivity detectors being upstream. Each set will be further subdivided into two groups to test the effect of filtering out the current spikes described in Sec. IV A.

Figure 4 shows that a histogram of 933 unfiltered measurements for set I is well fitted by a Gaussian curve. A χ^2 test yields $\chi^2=15.75$ for 16 degrees of freedom, corresponding to a 55% confidence level. A similar group of unfiltered measurements was obtained for set II with the results

$$r'_{\rm I}=1.267\,644\,931\pm0.000\,013\,680 ,$$

$$r'_{\rm II}=1.267\,672\,337\pm0.000\,012\,227 .$$

The Gaussian shape and a comparison with the filtered

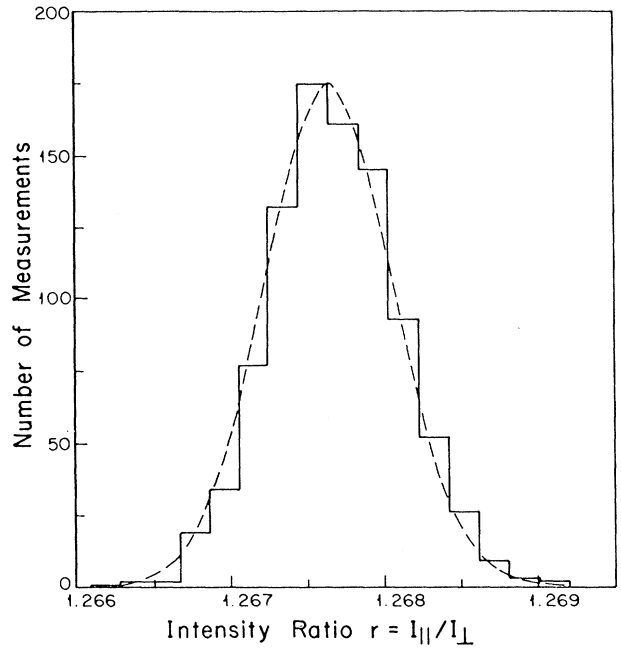

FIG. 4. Histogram for the distribution of the 933 unfiltered measurements of the intensity ratio $r'_{\rm I}$. The dotted line is a Gaussian distribution with the same mean and half-width.

results shows that the only observed result of the current spikes is to increase the standard deviation, without changing the mean value. Figure 5 shows a histogram for the 3019 filtered measurements from set I. The standard deviation is 30% smaller than what it would have been without filtering, but the average values for sets I and II,

$$r''_{\rm I}=1.267\,646\,870\pm0.000\,005\,555 ,$$

$$r''_{\rm II}=1.267\,656\,719\pm0.000\,005\,657 ,$$

agree with the above unfiltered values. Also, the χ^2 test improves to $\chi^2=21.60$ for 25 degrees of freedom, corresponding to a 67% confidence level. Since the standard deviation is proportional to $\sqrt{N}$, where N is the number of measurements, filtering reduces the number of measurements required for a given accuracy by nearly a factor of 2.

The weighted mean values for the two groups of measurements in each set are

$$r_{\rm I}=1.267\,646\,596\pm0.000\,005\,147 ,$$

$$r_{\rm II}=1.267\,659\,351\pm0.000\,005\,134 .$$

The corresponding uncorrected anisotropies are

$$R_{\rm I}=0.118\,028\,354\pm0.000\,002\,002 ,$$

$$R_{\rm II}=0.118\,033\,315\pm0.000\,001\,996 .$$

Averaging these gives the final uncorrected experimental value

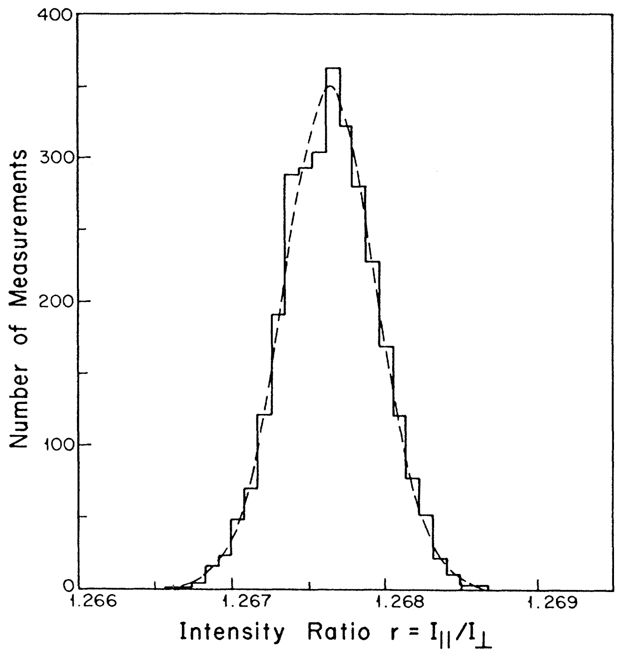

FIG. 5. Histogram for the distribution of the 3019 measurements of the intensity ratio r_{I}'', filtered to remove current spikes (see Sec. IV A). The dotted line is a Gaussian distribution with the same mean and half-width.

$$R_{\mathrm{expt}}=0.118\,030\,834\pm0.000\,001\,414$$

at a field strength of 631.05 V/cm.

The above difference of $(4.96\pm2.00)\times10^{-6}$ between R_{I} and R_{II} is in accord with the expected difference due to the different sensitivities of the detectors (see Sec. V B 2).

B. Systematic corrections

The above experimental value for the anisotropy includes the correction for background noise of about 0.2%. There remain further corrections for a small $2E1$ two-photon component of the signal, as well as corrections for averaging the signal over the finite solid angle of the detectors, beam bending and a relativistic angular shift. These are now discussed in the following subsections.

1. Two-photon background

The quenching signal contains a small isotropic background from the spontaneous $2E1$ decay of the $2\,^2S_{1/2}$ state. This can be calculated and subtracted provided that the sensitivity of the detectors to the broad two-photon continuum is known. For each detector, the photoelectron current due to $2E1$ transitions can be written in the form

$$I_{2E1}=\frac{I_a\gamma_{2s}}{2\gamma(F)}\int_0^{\nu}\eta(\nu)g(\nu)d\nu\ , \tag{61}$$

where $I_a=(I_{\parallel}+2I_{\perp})/3$ is an average intensity which is proportional to the total quench rate, independent of the anisotropy [cf. Eq. (29)], $\gamma_{2s}=131.7\ \mathrm{sec}^{-1}$ is the $2E1$ decay rate[24] and

$$\gamma(F)=\gamma_{2p}(eF)^2\left[\frac{|\langle 2s_{1/2}|z|2p_{1/2}\rangle|^2}{\mathcal{L}^2+\Gamma^2/4}+\frac{|\langle 2s_{1/2}|z|2p_{3/2}\rangle|^2}{\mathcal{F}^2+\Gamma^2/4}\right] \tag{62}$$

is the field-induced decay rate[11] to the ground state. The quantity $g(\nu)$ in (61) is the spectral distribution function for two-photon emission normalized so that

$$\tfrac{1}{2}\int_0^{\nu_0}g(\nu)d\nu=1\ ,$$

TABLE III. Systematic and higher-order corrections used to obtain the zeroth-order anisotropy R_0 and the Lamb shift $\mathcal{L}$ from R_{expt}.

Quantity	Value
Measured anisotropy R_{expt}	0.118 030 834(1414)
Detector nonlinearity	0.000 000 000(350)
$2E1$ two-photon decay	0.000 001 641(160)
Finite solid angle of detectors and deflections of ion beam	0.000 151 984(262)
Relativistic angular shift	0.000 007 499(12)
20.5 G Zeeman splitting	0.000 000 279(1)
$\mathbf{v}\times\mathbf{B}$ electric field	0.000 000 352(2)
$R_2F^2+R_4F^4$	−0.000 232 242(60)
$R_0(\delta R/R_0)_{M2}$	0.000 007 715
$R_0(\delta R/R_0)_n$	0.000 002 796
$R_0(\delta R/R_0)_n$	−0.000 000 755
R_0 (sum of above)	0.117 970 103(1489)
$\mathcal{L}$ [from Eqs. (31) and (33)]	14 042.59(18) MHz

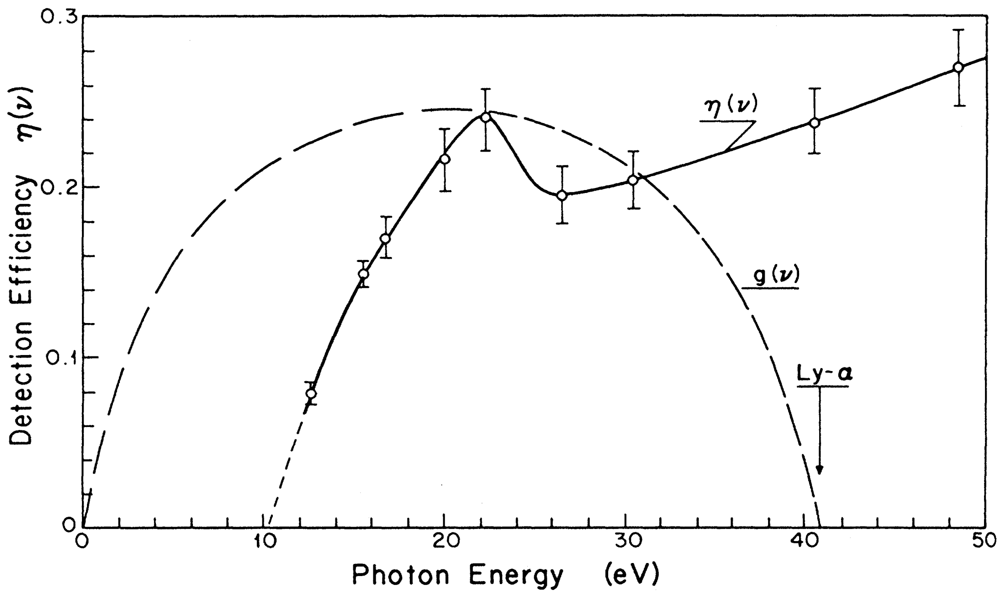

FIG. 6. Composite diagram showing the photosensitivity $\eta(\nu)$ for MgF_2 as a function of photon frequency (Ref. 25), and the $2E1$ $2s\,^2S_{1/2}$-$1s\,^2S_{1/2}$ two-photon distribution function $g(\nu)$ in arbitrary units (Ref. 24).

where $h\nu_0=E(2s_{1/2})-E(1s_{1/2})$ is the Lyα transition energy, and $\eta(\nu)$ is the sensitivity of the detector to photons of frequency ν relative to the sensitivity at ν_0. The factor of $\frac{1}{2}$ is included because each pair of photons is only counted once. The above assumes that, because of the small solid angle observed by the detectors, only one of each photon pair is recorded. The fractional correction to $R_{\rm expt}$ is then

$$\left[\frac{\delta R}{R}\right]_{2E1}=\left[\frac{\gamma_{2s}}{\gamma(F)}\right]\bar{\eta}(1+R/3)\ , \quad (63)$$

where

$$\bar{\eta}=\frac{1}{2\eta(\nu_0)}\int_0^{\nu_0}\eta(\nu)g(\nu)d\nu\ . \quad (64)$$

The function $g(\nu)$ shown in Fig. 6 is accurately known from theoretical calculations.[24] What remains to be found is $\eta(\nu)$ for the MgF_2 coating on the photosensitive cones for an angle of incidence of 42°, corresponding to the 96° cone angle. The experimental points in Fig. 6 are from the work of Lapson and Timothy[25] on the photon efficiency for MgF_2-coated channeltron electron multipliers at an angle of incidence of 45°. This can be taken to be the $\eta(\nu)$ for MgF_2 itself for the following reasons. First, a channeltron responds with near certainty to a single photoelectron. Second, the results for the coated channeltron are in agreement with the direct efficiency measurements on MgF_2 at an angle of incidence of 50° by Lukerskii *et al.*[26] for photon energies above 100 eV. Since only relative efficiencies are required to evaluate $\bar{\eta}$, small variations in angle are of negligible importance.

A numerical evaluation of the integral of Eq. (64) with the data shown in Fig. 6 yields the result $\bar{\eta}=0.637\pm0.065$. The estimated error corresponds to variations in the shape of $\eta(\nu)$ allowed by the error bars. $\eta(\nu)$ is known to be small below 10 eV (Ref. 25) where the curve extrapolates to zero. Using $\gamma_{2s}/\gamma(F)=2.102\times10^{-5}$ at $F=631.05$ V/cm, the correction to the anisotropy from Eq. (63) is $\delta R=(1.641\pm0.160)\times10^{-6}$ as listed in Table III.

2. *Finite solid angle and beam bending*

The solid angle correction takes into account the finite slit sizes of the photon collimators, along with the effects of beam deflection by the quenching field and the progressive depletion of the metastable state along the beam. Once the corrections have been obtained for a single detector, they must be averaged over the detector pairs shown in Fig. 3 with weighting factors w_1 and w_2 equal to the relative radiation intensities.

The radiation intensity decays exponentially along the beam according to $I(y)=I(0)e^{-\gamma y}$, where $1/\gamma$ is the decay length due to quenching. The beam also bends due to the transverse electric field in the z direction, giving it a parabolic trajectory of the form

$$z=z_0+\lambda y+\mu y^2\ , \quad (65)$$

where z_0 is the beam deflection and $\lambda=v_z/v_y$ is the velocity ratio in the z and y directions, all evaluated at the center of the detector viewing region. Finally, $\mu=|\mathbf{E}|/4V_a$, where V_a is the accelerating potential for the ion beam. In terms of these constants and the ones shown in Figs. 1 and 3, the observed anisotropy R is related to the solid angle corrected anisotropy R_c by

$$\frac{R}{R_c}=1-\frac{p^2}{2s^2}-\left[\frac{1-R_c}{s^2}\right]t^2\left[\frac{\alpha^2}{3}+\frac{\beta^2}{4}\right]-\frac{\beta^2}{2s^2}+\frac{\tilde{z}_0^2}{R_c s^2}[\tfrac{9}{4}(1-R_c^2)-R_c]-\frac{\tilde{\tilde{z}}_0^2}{R_c s^2}(1-R_c^2)\ , \qquad (66)$$

where

$$\tilde{z}_0^2=z_0^2+[\lambda^2+2(\mu-\lambda\gamma)z_0]\left[\frac{\alpha^2t^2}{3}+\frac{\beta^2(1-t^2)}{4}\right],$$

$$\tilde{\tilde{z}}_0^2=z_0^2+\tfrac{1}{2}[\lambda^2+2(\mu-\lambda\gamma)z_0]\left[\alpha^2t^2+\frac{\beta^2(3t^2+6t+2)}{4}\right]$$

and $t=s/d$. Equation (66) assumes that the signals from opposite detectors are averaged so that first-order corrections from beam bending cancel out. The input parameters for Eq. (66) and their uncertainties, along with the resulting relative errors $\delta R/R$ in the anisotropy, are listed in Table IV. The subscripts 1 and 2 on the parameters relating to beam bending refer to the upstream and downstream detector sets, respectively, in Fig. 3. The two correction factors are

$$(R_c/R)_1=1.001\,329\,298\pm0.000\,002\,006\ ,$$

$$(R_c/R)_2=1.001\,229\,248\pm0.000\,002\,116\ .$$

The difference $\Delta R_{1,2}/R=(1.000\,50\pm0.029\,42)\times10^{-4}$, corresponding to $\Delta R_{1,2}=11.81\times10^{-5}$, arises from the greater beam bending at the downstream position. The average of $(R_c/R)_1$ and $(R_c/R)_2$, weighted by the relative intensities w_1 and w_2 (see Table IV) at the two detector positions, is

$$(R_c/R)=1.001\,287\,647\pm0.000\,002\,0887\ .$$

This is the final value used to calculate the solid angle correction in Table III.

Since the signals from the upstream and downstream detectors were combined, the above difference could not be observed directly; but it could be observed indirectly when the two detector sets were interchanged. Our 30% difference in detector sensitivity corresponds to a predicted $\Delta R=(3.55\pm0.10)\times10^{-6}$ upon interchange. This is in good agreement with the observed value $(4.96\pm2.00)\times10^{-6}$ presented in Sec. V A.

3. *Relativistic angular shifts*

The observed intensity $I_{\parallel}$ emitted parallel to **E** in the laboratory frame by the fast moving ions corresponds to emission at a small angle $\theta=v/c$ to **E** in the comoving atomic frame. There is a similar angular shift for $I_{\perp}$, but because of rotational symmetry about the field direction, this intensity is not affected. The net correction to the anisotropy is

$$\delta R=R_c(1-R_c)(v/c)^2\ . \qquad (67)$$

4. *Zeeman splitting and* $\mathbf{v}\times\mathbf{B}$ *fields*

The Zeeman splittings of the $n=2$ manifold of states in an axial magnetic field **B** produce corrections to the mixing coefficients $a(F)$ and $b^{(j)}_{m,m'}(F)$ in Eq. (8) which cancel out to first order in $|\mathbf{B}|$. However in second order, the net effect is to enhance the Stark coupling between the $2\,^2S_{1/2}$ and $2\,^2P_{1/2}$ sublevels, thereby decreasing the anisotropy. For our field strength of 20.5 G, the correction to R is $\delta R=(0.279\pm0.001)\times10^{-6}$.

The **B** field introduces a further correction. As the ion beam traverses the quenching field **E**, it progressively acquires a velocity component $v_z=\lambda v_y$ [see Eq. (65)] in the transverse direction. The resulting $\mathbf{v}\times\mathbf{B}$ electric field is perpendicular to **E**, and the vector sum produces a net effective quenching field which is rotated through a small angle $\theta=v_zB/(cF)$. The resulting correction to the anisotropy is

$$\delta R/R_c=2\theta^2\ . \qquad (68)$$

This must be evaluated separately for the upstream and downstream detectors.

Numerical values for the above corrections and the final experimental value for the zeroth-order anisotropy R_0 are summarized in Table III. The Lamb shift $\mathcal{L}$ is then obtained from R_0 using Eqs. (31) and (33).

TABLE IV. Parameters for calculating the solid angle and beam bending corrections [see Eq. (66)]. $\delta R/R$ is the relative error in R corresponding to the uncertainty in each parameter.

Parameter	Value	$\delta R/R$ (ppm)
α	0.6223 ± 0.0013 cm	1.051
β	0.6350 ± 0.0013 cm	1.641
c	7.1171 ± 0.0025 cm	0.082
d	14.8826 ± 0.0025 cm	0.396
p	0.1143 ± 0.0077 cm	0.092
μ	$(1.178\pm0.010)\times10^{-3}$ cm^{-1}	0.003
λ_1	$0.011\,74\pm0.0009$	0.004
λ_2	$0.018\,92\pm0.0015$	0.007
$(z_0)_1$	$0.030\,34\pm0.000\,24$ cm	0.177
$(z_0)_2$	$0.077\,06\pm0.000\,62$ cm	0.835
w_1	0.5745 ± 0.0010	0.000
w_2	0.4255 ± 0.0010	0.000
γ	$0.098\,53\pm0.0080$ cm^{-1}	0.000

VI. DISCUSSION

The final experimental value for the Lamb shift from Table III is $14\,042.59\pm0.18$ MHz, as first reported in Ref. 27. This agrees with, but is somewhat higher than our previous anisotropy measurement[4] of $14\,042.22\pm0.35$ MHz. The statistically weighted mean of the two measurements is $14\,042.52\pm0.16$ MHz. This is in good agreement with the currently best microwave resonance

TABLE V. Comparison of theory and experiment for the He^+ Lamb shift (in MHz).

Experiment	Theory
14042.51 ± 0.16[a]	14042.33 ± 0.5[e]
14042.0 ± 1.2[b]	14042.51 ± 0.2[f]
14046.2 ± 1.2[c]	
14040.2 ± 1.8[d]	

[a]Present work.
[b]Reference 10.
[c]Reference 28.
[d]Reference 29.
[e]Calculated with Mohr's (Ref. 8) $\Delta G_{\rm SE}(Z\alpha)=-22.9(1.0)$.
[f]Calculated with revised $\Delta G_{\rm SE}(Z\alpha)=-22.48(38)$ (see the Appendix and Table VIII).

value of 14 042.0±1.2 MHz,[10] but is substantially more accurate. Table V gives a complete listing of past measurements. Only the older measurement of Narasimham and Strombotne[28] (14046.2±1.2 MHz) is in clear disagreement with the others.[29]

A recent discussion of Lamb shift calculations has been given by Sapirstein and Yennie.[30] To compare with theory, the energies of the $2s_{1/2}$ and $2p_j$ $(j=\frac{1}{2},\frac{3}{2})$ states can be written in the form

$$E(l,j)=E_D(j)+\Delta E_L(l,j)+\Delta E_M+\Delta E_{ns}\ , \tag{69}$$

where $E_D(j)$ is the Dirac energy, $\Delta E_L(l,j)$ is the QED correction for infinite nuclear mass, ΔE_M is the finite nuclear mass correction, and ΔE_{ns} is the finite nuclear size correction. The first two are given by[5,30,31] (for $n=2$)

$$E_D(j)=-\frac{(Z\alpha)^2mc^2}{N(N+2+\gamma-k)} \tag{70}$$

with $k=j+\frac{1}{2}$, $\gamma=[k^2-(Z\alpha)^2]^{1/2}$, and $N=2[1-(1-k/2)(k-\gamma)]^{1/2}$, and

$$\begin{aligned}\Delta E_L(l,j)=\mathcal{C}\big([\tfrac{19}{30}+\ln(Z\alpha)^{-2}]\delta_{l,0}-\beta_l+\tfrac{3}{8}\delta_{l,1}c_{l,j}/(2l+1)+\pi Z\alpha(\tfrac{427}{128}-\tfrac{1}{2}\ln2)\delta_{l,0}\\ +(Z\alpha)^2\{-\tfrac{3}{4}\ln^2(Z\alpha)^{-2}\delta_{l,0}+\ln(Z\alpha)^{-2}[(4\ln2-\tfrac{41}{120})\delta_{l,0}+(\tfrac{29}{120}+\tfrac{3}{16}\delta_{j,1/2})\delta_{l,1}]+G(Z\alpha)\}\\ +(\alpha/\pi)[0.4041\delta_{l,0}-0.2464\delta_{l,1}c_{l,j}/(2l+1)+O(Z\alpha)]+O(\alpha^2/\pi^2)\big)\ ,\end{aligned} \tag{71}$$

where $c_{l,j}=2(j-l)/(j+\frac{1}{2})$ is the anomalous magnetic moment factor and the overall multiplying factor is

$$\mathcal{C}=\alpha(Z\alpha)^4mc^2/6\pi=135.643\,81(2)Z^4\ \text{MHz}\ .$$

The Bethe logarithms are[7]

$$\beta_{2s}=2.811\,769\,893\,120,\quad \beta_{2p}=-0.030\,016\,708\,630\ .$$

The finite nuclear mass corrections consist of a reduced mass part, given to sufficient accuracy by

$$\begin{aligned}\Delta E_M(\text{red. mass})=-\frac{\mu}{M}\left[1-\frac{(Z\alpha)^2}{16}\right]E_D(j)+\left[\left[\frac{\mu}{m}\right]^3-1\right]\Delta E_L(l,j)\\ -\mathcal{C}\left[\ln(\mu/m)\delta_{l,0}-\left[\frac{\mu}{m}\right]^2\left[1-\frac{\mu}{m}\right]\tfrac{3}{8}\delta_{l,1}c_{l,j}/(2l+1)\big)\right]\ ,\end{aligned} \tag{72}$$

where $\mu=mM/(m+M)$ is the reduced mass, and a relativistic recoil part[32,33]

$$\Delta E_M(\text{rel. rec.})=\mathcal{C}(Z\mu/M)\{-2\beta_l+[\tfrac{1}{4}\ln(Z\alpha)^{-2}+\tfrac{187}{24}]\delta_{l,0}-\tfrac{7}{24}\delta_{l,1}\}\ . \tag{73}$$

The term proportional to $E_D(j)$ in Eq. (72) does not contribute to $\mathcal{L}$, but it does contribute to $\mathcal{F}$. There are additional radiative-recoil corrections of order $\mathcal{C}(Z\alpha\mu/M)$ and pure recoil corrections or order $\mathcal{C}(Z^2\alpha\mu/M)$. Evaluation of the latter has recently been completed.[34] The higher-order (HO) results for both sets of terms are

$$\Delta E_M(\text{HO})=\tfrac{3}{4}\mathcal{C}\pi(Z\alpha\mu/M)\{(\tfrac{35}{4}\ln2-\tfrac{39}{5}+\tfrac{31}{192}-0.415\pm0.004)+Z[\tfrac{5}{2}-\ln(2/Z\alpha)+2\ln(1/Z\alpha)-4.25]\}\delta_{l,0} \tag{74}$$

The total contribution from Eq. (74) is −0.016 MHz for $^4He^+$. The remaining nuclear size correction in Eq. (69) is

$$\Delta E_{ns}=\tfrac{1}{12}\alpha^2Z^4mc^2(r_{\rm rms}/a_0)^2\delta_{l,0} \tag{75}$$

where $r_{\rm rms}$ is the root-mean-square radius of the nuclear charge distribution. [For higher-Z ions, see Eq. (A23) in the Appendix.]

The nuclear size correction requires some additional discussion. In the case of Lamb shift measurements in hydrogen, this is a major source of uncertainty because there are two measurements of $r_{\rm rms}$ which differ by several times the quoted error bars [0.805 ± 0.011 fm (Ref. 35) and 0.862 ± 0.012 fm (Ref. 36)]. The corresponding difference in the Lamb shift is 18 kHz, which is twice the experimental uncertainty. The situation is more favorable in the case of He^+. Here, there have been three electron scattering measurements of $r_{\rm rms}$ which are in good agreement with each other.[37–39] The combined result of all three measurements is $r_{\rm rms}=1.674\pm0.012$ fm.[39] In addition, the value $r_{\rm rms}=1.673\pm0.001$ fm has been determined from the $2s_{1/2}-2p_{1/2}$ and $2s_{1/2}-2p_{3/2}$ transition frequencies of the muonic system μ^--He^{2+}.[40] The validity of this measurement has been questioned because of subsequent difficulties in observing evidence for the μ^--$\mathrm{He}^{2+}(2s)$ metastable state.[41–43] However, Bracci and Zavatinni[44] have recently argued that the observation of the muonic transition frequencies at high pressures (~ 40 atm) can be explained by the formation of triplet molecular ions of the form $\mathrm{He}(\mu^-$-$\mathrm{He}^{2+})$, analogous to the stable triplet HeH^+ molecule. In view of this, we take the muonic measurement of $r_{\rm rms}$ as correct. Reverting to the less accurate electron scattering value of $r_{\rm rms}$ has almost no effect on the final value for $\mathcal{L}$, but it increases the uncertainty in the nuclear size correction ΔE_{ns} by about a factor of 10. A remeasurement of the muonic transition frequencies at low pressure would be highly desirable for the interpretation of the electronic Lamb shift in He^+.[45–47]

The term $G(Z\alpha)$ in Eq. (71), which represents the sum of all higher-order terms in $Z\alpha$, consists of the self-energy and vacuum polarization parts

$$G(Z\alpha)=G_{\rm SE}(Z\alpha)+G_{\rm VP}(Z\alpha)\ . \tag{76}$$

The dominant source of theoretical uncertainty at low Z comes from the term $G_{\rm SE}(Z\alpha)$. The available calculations at $Z=10$, 20, and 30 (Ref. 48) have been extrapolated by Mohr[8] to low Z by fitting exactly a three-parameter function of the form

$$G_{\rm SE}(Z\alpha)=a_1+(Z\alpha)[a_2\ln(Z\alpha)^{-2}+a_3]\ . \tag{77}$$

For the $2s_{1/2}$ state of He^+, this procedure yields $G_{\rm SE}=-23.55\pm1.0$, where the uncertainty is determined by allowing the $Z=10$ value to shift by the amount of its uncertainty. The corresponding Lamb shift is $14\,042.33\pm0.5$ MHz. This agrees with experiment, although the central value lies lower by more than the experimental uncertainty. A more extended five parameter fit to all ten calculated points up to $Z=100$ is described in the Appendix. The result is the somewhat higher value $G_{\rm SE}=-23.16\pm0.15$ for the $2s_{1/2}$ state (or $\Delta G_{\rm SE}=-22.48\pm0.38$ for the transition), corresponding to a Lamb shift of $14\,042.51\pm0.2$ MHz. The additional uncertainty due to the nuclear size correction is ±0.02 MHz assuming the muonic value for $r_{\rm rms}$, and ±0.2 MHz assuming the electron scattering value. A further uncertainty of ±0.15 MHz assigned by Sapirstein and Yennie[49] due to uncalculated recoil corrections is no longer included because the evaluation of these terms is now complete.[34] The new terms are included in Eq. (74). The excellent agreement with experiment lends support to the higher value for $G_{\rm SE}$, but the question cannot be settled

TABLE VI. Comparison of theory and experiment for the total Lamb shift, and the derived electron self-energy part $G_{\rm SE}$ of the term $G(Z\alpha)$ in Eq. (1). $r_{\rm rms}$ is the nuclear radius used.

Ion	$r_{\rm rms}$ (fm)	$\mathcal{L}_{\rm expt}$	$\mathcal{L}_{\rm theor}$	$(\Delta G_{\rm SE})^a_{\rm expt}$	$(\Delta G_{\rm SE})_{\rm theor}$	$(\Delta G_{\rm VP})^b_{\rm theor}$
^{1}H	0.862(12)	1057.845(9)[c]	1057.878(8) MHz	$-27.45\pm1.25\pm0.57$	$-22.91(40)$	-0.516
	0.805(11)		1057.859(8) MHz	$-24.88\pm1.25\pm0.48$		
^{4}He	1.673(1)	14 042.52(16)[d]	14042.51(20)	$-22.47\pm0.35\pm0.02$	$-22.45(38)$	-0.508
^{6}Li	2.56(5)	62 765.(21)[e]	62739.(6)	$-17.22\pm4.0\pm0.78$	$-22.10(33)$	0.500
^{16}O	2.711(14)	2192.(15)[f]	2196.54(47) GHz	$-22.92\pm7.9\pm0.03$	$-20.52(22)$	-0.473
		2215.6(7.5)[g]		$-10.45\pm4.0\pm0.03$		
		2203.(11)[h]		$-17.11\pm5.8\pm0.03$		
^{19}F	2.900(15)	3339.(35)[i]	3343.7(9)	$-21.47\pm9.1\pm0.03$	$-20.24(20)$	-0.469
^{31}P	3.197(5)	20.188(29)[j]	20.258(11) THz	$-19.63\pm0.35\pm0.004$	$-18.75(13)$	-0.449
^{32}S	3.247(4)	25.266(63)[k]	25.378(16)	$-19.45\pm0.52\pm0.003$	$-18.53(12)$	-0.447
^{35}Cl	3.335(18)	31.19(22)[l]	31.35(2)	$-19.22\pm1.3\pm0.013$	$-18.31(12)$	-0.444
^{40}A	3.428(8)	37.89(38)[m]	38.25(2)	$-19.55\pm1.6\pm0.005$	$-18.09(10)$	-0.442
^{238}U	5.751(50)	70.4(8.3)[n]	75.3(4) eV	$-7.83\pm0.46\pm0.02$	$-7.563(4)$	$-0.600(8)$

[a]The first uncertainty listed is due to the experimental uncertainty in $\mathcal{L}$, and the second to the nuclear radius uncertainty.
[b]$\Delta G_{\rm VP}=\Delta G_U+\Delta G_{\rm WK}$.
[c]Reference 9.
[d]Present work.
[e]Reference 50.
[f]Reference 51.
[g]Reference 52.
[h]Reference 53.
[i]Reference 54.
[j]Reference 55.
[k]Reference 56.
[l]Reference 57.
[m]Reference 58.
[n]Reference 59.

until more accurate calculations are available for low Z.

For hydrogen, the revised fit increases G_{SE} from -24.1 ± 1.2 to -23.60 ± 0.17. The effect is to increase the Lamb shift by 4 kHz to 1057.859(8) MHz for $r_{rms}=0.805$ fm and 1057.878(8) MHz for $r_{rms}=0.862$ fm. Both of these lie above the experimental value[9] of 1057.845(9) MHz.

The next largest source of uncertainty due to uncalculated terms in the Lamb shift arises from the exchange of two virtual photons. This gives rise to the leading terms of order $\mathcal{O}(\alpha/\pi)$ in Eq. (71) [denoted by B_{40} in Eq. (1)], but binding corrections of relative order $Z\alpha B_{50}$ have not been evaluated. Assuming a coefficient $B_{50}\simeq\pm2B_{40}$, the uncertainty in $\mathcal{L}$ is $\pm2Z^5$ kHz for low Z. The result for He^+ is ±0.06 MHz.

Since the primary theoretical uncertainty comes from the G_{SE} part of $G(Z\alpha)$ in Eq. (76), it is instructive to extract an experimental value for G_{SE} from the measurements by taking the other well-established terms in Eq. (1) as correct and subtracting their contributions. The results for all ions for which measurements of significant precision are available are shown in Table VI, along with the values of the nuclear radii used and their uncertainties. The tabulated quantity is $\Delta G_{SE}=G_{SE}(2s_{1/2})-G_{SE}(2p_{1/2})$ for the Lamb shift transition. Other details of the calculations as a function of Z are given in the Appendix. (Not included in the table is the work of Sokolov and co-workers[60] who effectively measure the ratio $\mathcal{L}/\Gamma_p$ to very high precision.) Our value for He^+ of $\Delta G_{SE}=-22.47\pm0.35$, together with the values for P^{14+} and S^{15+} of -19.63 ± 0.35 and -19.45 ± 0.52, respectively, provide the most stringent tests of theory. While the former is in agreement with theory, the latter two lie significantly below theory. Most of the results for $Z\geq8$ show a similar trend. Since the other theoretical terms are assumed to be correct, the uncertainties in the above experimentally derived values for ΔG_{SE} reflect only the experimental errors in $\mathcal{L}$ an r_{rms}. There is an additional uncertainty of $\pm0.2/Z$ for small Z due to the uncalculated two-photon exchange term B_{50} discussed above. This is much less than what is required to reconcile the apparent agreement with theory for He^+ with the above disagreement at higher Z.

In summary, the 11-ppm accuracy obtained in the present work for He^+ rivals the 9-ppm accuracy in hydrogen.[9] The He^+ result is a factor of 4 more sensitive to the $G(Z\alpha)$ term because of its Z^2 scaling relative to the leading terms. The interpretation of the results is relatively unaffected by uncertainties in the nuclear size correction, even if the less accurate electron scattering value of τ is used. The derived value for $\Delta G_{SE}(Z\alpha)$ is in good agreement with theory, especially with the revised value obtained in the Appendix by fitting to all the calculations up to $Z=100$. The most pressing problems for future work are (i) improved calculations of G_{SE} for low Z and (ii) a remeasurement of the μ^--He^{2+} transition frequencies at low pressure in order to determine a firm value for r_{rms}.

ACKNOWLEDGMENTS

Research support by the Natural Sciences and Engineering Research Council of Canada is gratefully acknowledged. One of us (G.W.F.D.) wishes to thank the Killam Foundation for support.

APPENDIX

Values of $G_{SE}(Z\alpha)$ for $Z<10$ have been obtained in the past by fitting exactly a three-parameter function of the form of Eq. (77) to calculations at $Z=10$, 20, and 30. However, there is additional information contained in the results for $Z=40, 50, \ldots, 100$ which might be used to advantage, especially in view of the large uncertainty introduced by the calculation for $Z=10$. To this end, we have tried fitting the five-parameter function

$$f(x)=a_1+a_2x\ln x^{-2}+a_3x+a_4x^2+a_5x^M\ , \tag{A1}$$

where M is an integer in the range 8–15 chosen to give the best overall fit to the data. The last term provides a phenomenological representation of the strongly nonperturbative behavior of the self-energy which eventually sets in for high Z, but it makes a negligible contribution for low Z. The final results for low Z are nearly independent of M over a broad range. The above five functions provide an accurate representation over the entire range of Z without oversaturating the function space so that the coefficients become only weakly determined. Since

TABLE VII. Fit to $G_{SE}(Z\alpha)$ derived from Mohr's[8] electron self-energy term $F(Z\alpha)$ for the $2s_{1/2}$ state.

Z	$F(Z\alpha)$	$G_{SE}(Z\alpha)$	Fit, Eq. (A9)	Difference
10	4.893(2)	-20.69 ± 0.28	-20.54	-0.15
20	3.5063(4)	-18.114 ± 0.014	-18.109	-0.005
30	2.8391(3)	-16.101 ± 0.005	-16.103	0.002
40	2.4550(3)	-14.351 ± 0.003	-14.351	-0.0004
50	2.2244(2)	-12.771 ± 0.001	-12.771	-0.0002
60	2.0948(4)	-11.316 ± 0.002	-11.317	0.0005
70	2.0435(8)	-9.956 ± 0.002	-9.956	0.0002
80	2.065(2)	-8.664 ± 0.004	-8.663	-0.0007
90	2.169(3)	-7.411 ± 0.005	-7.411	0.0004
100	2.387(3)	-6.160 ± 0.004	-6.160	-0.0000

the revised fit has a noticeable effect on the comparison with experiment, the procedure is described below in some detail.

The coefficients a_i are determined by a least-squares fit. Defining the basis set of functions

$$f_1(x)=1,\quad f_2(x)=x\ln x^{-2},$$
$$f_3(x)=x,\quad f_4(x)=x^2,\quad f_5(x)=x^M,$$

the least-squares solution for the column vector of coefficients **a** is[61]

$$\mathbf{a}=\underline{A}^{-1}\mathbf{b},\tag{A2}$$

where

$$A_{kj}=\sum_{i=1}^{10}\frac{f_j(Z_i\alpha)f_k(Z_i\alpha)}{\sigma_i^2},\tag{A3}$$

$$b_k=\sum_{i=1}^{10}\frac{G_{\rm SE}(Z_i\alpha)f_k(Z_i\alpha)}{\sigma_i^2},\tag{A4}$$

$Z_i=10, 20, \ldots, 100$ for $i=1,2,\ldots,10$ and σ_i is the uncertainty in the calculated $G_{\rm SE}(Z_i\alpha)$. The quantity $F(Z\alpha)$ tabulated by Mohr[48] is the total self-energy summed to all orders in $Z\alpha$. It is related to $G_{\rm SE}(Z\alpha)$ by

$$G_{\rm SE}(Z\alpha)=[\tfrac{3}{4}F(Z\alpha)-F_{\rm low}(Z\alpha)]/(Z\alpha)^2,\tag{A5}$$

where $F_{\rm low}(Z\alpha)$ contains the known low-order terms which must be subtracted. They are

$$F_{\rm low}(Z\alpha)=\ln(Z\alpha)^{-2}+\tfrac{19}{30}-\beta_{nl}+6.968\,340\,681(Z\alpha)+(Z\alpha)^2[-\tfrac{3}{4}\ln^2(Z\alpha)^{-2}+A_{61}(n,l,j)\ln(Z\alpha)^{-2}]\tag{A6}$$

for s states and

$$F_{\rm low}(Z\alpha)=-\beta_{nl}+\tfrac{3}{8}c_{l,j}/(2l+1)+A_{61}(n,l,j)(Z\alpha)^2\ln(Z\alpha)^{-2}\tag{A7}$$

for p states. The values of $A_{61}(n,l,j)$ are

$$A_{61}(1,0,\tfrac{1}{2})=7\ln2-\tfrac{63}{80},\quad A_{61}(2,0,\tfrac{1}{2})=4\ln2+\tfrac{67}{40},$$
$$A_{61}(2,1,\tfrac{1}{2})=\tfrac{103}{240},\quad A_{61}(2,1,\tfrac{3}{2})=\tfrac{29}{120}.$$

Correspondingly, $\sigma_i=\frac{3}{4}\sigma_i^{(F)}/(Z_i\alpha)^2$, where $\sigma_i^{(F)}$ is the uncertainty in $F(Z_i\alpha)$. The results of the least-squares fit are

$$G_{\rm SE}(1s_{1/2};Z\alpha)=-23.419+5.852Z\alpha\ln(Z\alpha)^{-2}+15.922Z\alpha+4.294(Z\alpha)^2+2.572(Z\alpha)^{15},\tag{A8}$$
$$G_{\rm SE}(2s_{1/2};Z\alpha)=-24.177+6.293Z\alpha\ln(Z\alpha)^{-2}+16.548Z\alpha+5.549(Z\alpha)^2+2.977(Z\alpha)^{11},\tag{A9}$$
$$G_{\rm SE}(2p_{1/2};Z\alpha)=-0.715+0.170Z\alpha\ln(Z\alpha)^{-2}+1.195Z\alpha+0.357(Z\alpha)^2+1.502(Z\alpha)^{8},\tag{A10}$$
$$G_{\rm SE}(2p_{3/2};Z\alpha)=-0.417+0.233Z\alpha\ln(Z\alpha)^{-2}+0.449Z\alpha+0.191(Z\alpha)^2-0.032(Z\alpha)^{7}.\tag{A11}$$

As an example, the details of the fit for the $2s_{1/2}$ state are shown in Table VII. In each case, the deviations from the input points are substantially less than the uncertainties. The accuracy of the result $G_{\rm SE}(2s_{1/2})=-23.16$ for $Z=2$ was determined by (i) letting the calculated points shift up and down by $\pm\sigma_i$, (ii) deleting each of the points in turn from the fit, and (iii) progressively deleting all the points for $Z=10$, 20, and 30. In no case did the extrapolated value at $Z=2$ change by more than ±0.1. Changing M in the range $8\le M\le 14$ also gave agreement to within ±0.1. However, these tests may still underestimate the actual error. To be conservative, we take the uncertainty to be three times the change in $G_{\rm SE}$ from test (i) above. Even this may underestimate errors introduced by the empirical form of the fit at high Z. A definitive value must await accurate calculations at low Z.

The difference from previous extrapolations comes primarily from the choice of weights. Setting $\sigma_i=1$ in (A3) and (A4) yields $G_{\rm SE}(2s_{1/2})=-23.56\pm0.75$ for $Z=2$, in close agreement with Mohr's[8] estimate, but with somewhat reduced error. However, this procedure gives much higher weight to the $Z=10$ calculation than is justified by its accuracy. Omitting this point from the fit yields -23.20, in agreement (±0.1) with our revised value. For the $1s_{1/2}$ state, the difference is much less and in the opposite direction, the values for $Z=2$ being -22.35 Mohr's procedure and -22.46 from Eq. (A8).

A similar fit can be obtained for the Uehling vacuum polarization contribution denoted by Mohr[8] as $H_U(Z\alpha)$. $H_U(Z\alpha)$ is related to $G_U(Z\alpha)$ by

$$G_U(Z\alpha)=[\tfrac{3}{4}H_U(Z\alpha)-H_{\rm low}(Z\alpha)]/(Z\alpha)^2,\tag{A12}$$

where

$$H_{\rm low}(Z\alpha)=-\tfrac{1}{5}+(5\pi/64)(Z\alpha)-\tfrac{1}{10}(Z\alpha)^2\ln(Z\alpha)^{-2}\tag{A13}$$

for s states and $H_{\rm low}(Z\alpha)=0$ for p states. Since a_1 is known exactly,[30] only the remaining four parameters in (A1) need be fitted. With $\sigma_i=1$, the results are

TABLE VIII. Summary of values used for $G_{\rm SE}(Z\alpha)$, $G_U(Z\alpha)$, and $G_{\rm WK}(Z\alpha)$, as calculated from Eqs. (A8)–(A21).

State	$G_{\rm SE}(Z\alpha)$	$G_U(Z\alpha)$	$G_{\rm WK}(Z\alpha)$
H($1s_{1/2}$)	−22.88(27)	−0.464	0.042
H($2s_{1/2}$)	−23.60(17)	−0.606	0.042
H($2p_{1/2}$)	−0.69(23)	−0.048	0
H($2p_{3/2}$)	−0.40(21)	−0.011	0
He$^+$($1s_{1/2}$)	−22.46(25)	−0.455	0.041
He$^+$($2s_{1/2}$)	−23.16(15)	−0.597	0.041
He$^+$($2p_{1/2}$)	−0.68(23)	−0.048	0
He$^+$($2p_{3/2}$)	−0.38(21)	−0.011	0

$$G_U(1s_{1/2};Z\alpha)=-0.475\,180+0.163\,99Z\alpha\ln(Z\alpha)^{-2}-0.025\,17Z\alpha-0.155\,52(Z\alpha)^2-1.064\,82(Z\alpha)^8\ , \qquad (A14)$$

$$G_U(2s_{1/2};Z\alpha)=-0.619\,167+0.168\,75Z\alpha\ln(Z\alpha)^{-2}+0.113\,93Z\alpha-0.541\,18(Z\alpha)^2-2.467\,01(Z\alpha)^8\ , \qquad (A15)$$

$$G_U(2p_{1/2};Z\alpha)=-0.048\,214-0.005\,53Z\alpha\ln(Z\alpha)^{-2}-0.056\,14Z\alpha-0.232\,03(Z\alpha)^2-1.157\,99(Z\alpha)^8\ , \qquad (A16)$$

$$G_U(2p_{3/2};Z\alpha)=-0.010\,714+0.001\,15Z\alpha\ln(Z\alpha)^{-2}+0.008\,29Z\alpha-0.005\,60(Z\alpha)^2+0.001\,62(Z\alpha)^8\ . \qquad (A17)$$

A fit to the Wichmann-Kroll vacuum polarization calculations of Johnson and Soff,[31] using an extension of the functional forms given by Mohr,[62] yields

$$G_{WK}(1s_{1/2};Z\alpha)=0.042\,51-0.103\,05Z\alpha+(Z\alpha)^2[0.047\,93\ln(Z\alpha)^{-2}+0.129\,30-0.068\,26Z\alpha\ln(Z\alpha)^{-2}]\ , \qquad (A18)$$

$$G_{WK}(2s_{1/2};Z\alpha)=0.042\,51-0.103\,05Z\alpha+(Z\alpha)^2[0.044\,63\ln(Z\alpha)^{-2}+0.175\,12-0.103\,96Z\alpha\ln(Z\alpha)^{-2}]\ , \qquad (A19)$$

$$G_{WK}(2p_{1/2};Z\alpha)=(Z\alpha)^2[0.001\,13\ln(Z\alpha)^{-2}+0.054\,31-0.058\,78Z\alpha\ln(Z\alpha)^{-2}]\ , \qquad (A20)$$

$$G_{WK}(2p_{3/2};Z\alpha)=(Z\alpha)^2[0.001\,13\ln(Z\alpha)^{-2}+0.002\,12-0.000\,98Z\alpha\ln(Z\alpha)^{-2}]\ . \qquad (A21)$$

The total vacuum polarization term is then

$$G_{VP}(Z\alpha)=G_U(Z\alpha)+G_{WK}(Z\alpha)\ . \qquad (A22)$$

The final values used for $G_{SE}(Z\alpha)$, $G_U(Z\alpha)$, and $G_{WK}(Z\alpha)$ are summarized in Table VIII. All of the above assume a point nuclear charge distribution. The accuracies of the fits for $G_U(Z\alpha)$ and $G_{WK}(Z\alpha)$ are much better than the uncertainties in $G_{SE}(Z_i\alpha)$.

For the finite nuclear size correction, Eq. (75) is adequate for low-Z spins, but there are important relativistic corrections for high-Z ions as discussed by Mohr.[62] There are also significant finite-size corrections $(\Delta E_{ns})_{SE}$ and $(\Delta E_{ns})_U$ to the self-energy and Uehling vacuum polarization terms calculated by Johnson and Soff.[31] The total finite-size correction is therefore written in the form

$$\Delta E_{ns}=\tfrac{2}{3}n^{-3}[\delta_{l,0}+t_{n,l}(Z\alpha)^2](Z\alpha)^2(Zr_{rms}/a_0)^{2s}mc^2 + (\Delta E_{ns})_{SE}+(\Delta E_{ns})_U\ , \qquad (A23)$$

where $s=[1-(Z\alpha)^2]^{1/2}$ and $t_{1s}=0.50$, $t_{2s}=1.38$, $t_{2p,1/2}=3/16$, $t_{2p,3/2}=0$. In Table VI, the terms $(\Delta E_{ns})_{SE}$ and $(\Delta E_{ns})_U$ are negligible except in the case of U^{91+}, where they contribute

$$(\Delta E_{ns})_{SE}+(\Delta E_{ns})_U=-1.1189+0.831=-0.358\ \text{eV}\ .$$

*Permanent address: Institute of Experimental Physics, University of Gdańsk, 80-952 Gdańsk, Poland.

[1]G. W. F. Drake and R. B. Grimley, Phys. Rev. A **8**, 157 (1973); A. van Wijngaarden, G. W. F. Drake, and P. S. Farago, Phys. Rev. Lett. **33**, 4 (1974).

[2]G. W. F. Drake, S. P. Goldman, and A. van Wijngaarden, Phys. Rev. A **20**, 1299 (1979).

[3]J. Patel, A. van Wijngaarden, and G. W. F. Drake, Phys. Rev. A **36**, 5130 (1987).

[4]G. W. F. Drake, J. Patel, and A. van Wijngaarden, Phys. Rev. Lett. **60**, 1002 (1988).

[5]G. W. F. Drake, Adv. At. Mol. Phys. **18**, 399 (1982).

[6]S. E. Haywood and J. D. Morgan III, Phys. Rev. A **32**, 3179 (1985).

[7]G. W. F. Drake and R. A. Swainson, Phys. Rev. A **41**, 1243 (1990).

[8]P. J. Mohr, Phys. Rev. A **26**, 2338 (1982), and in *Beam Foil Spectroscopy,* edited by I. A. Sellin and D. J. Pegg (Plenum, New York, 1976), p. 89.

[9]S. R. Lundeen and F. M. Pipkin, Metrologia **22**, 9 (1986).

[10]M. S. Dewey and R. W. Dunford, Phys. Rev. Lett. **60**, 2014 (1988).

[11]G. W. F. Drake, in *Spectrum of Atomic Hydrogen: Advances,* edited by G. W. Series (World Scientific, Singapore, 1988).

[12]G. W. F. Drake, in *Spectrum of Atomic Hydrogen: Advances* (Ref. 11), pp. 232–236.

[13]W. E. Lamb Jr. and R. C. Retherford, Phys. Rev. **79**, 1549 (1950); W. E. Lamb, *ibid.* **85**, 259 (1952).

[14]V. Weisskopf and E. Wigner, Z. Phys. **63**, 54 (1930).

[15]E. J. Kelsey and J. Macek, Phys. Rev. A **16**, 1322 (1977).

[16]M. Hillery and P. J. Mohr, Phys. Rev. A **21**, 24 (1980).

[17]A. van Wijngaarden and G. W. F. Drake, Phys. Rev. A **17**, 1366 (1978).

[18]A. van Wijngaarden and G. W. F. Drake, Phys. Rev. A **25**, 400 (1982).

[19]A. R. Edmonds, *Angular Momentum in Quantum Mechanics* (Princeton University Press, Princeton, NJ, 1960).

[20]G. W. F. Drake, Phys. Rev. A **3**, 908 (1971); G. Feinberg and J. Sucher, Phys. Rev. Lett. **26**, 681 (1971); I. L. Beigman and U. I. Safranova, Zh. Eksp. Teor. Fiz. **60**, 2045 (1971) [Sov. Phys.—JETP **33**, 1102 (1971)].

[21]M. Cohen and A. Dalgarno, Proc. R. Soc. London, Ser. A **280**, 258 (1964); **293**, 359 (1966). See also Ref. 12.

[22]J. P. Lévy, Phys. Rev. A **29**, 3189 (1984).

[23]Keithley Co. (private communication).

[24]S. P. Goldman and G. W. F. Drake, Phys. Rev. A **24**, 183 (1981); F. A. Parpia and W. R. Johnson, *ibid.* **26**, 1142 (1982); G. W. F. Drake, *ibid.* **34**, 2871 (1986).

[25]L. B. Lapson and J. G. Timothy, Appl. Opt. **12**, 388 (1973); **15**, 1218 (1976).

[26]A. P. Lukirskii, E. P. Savinov, I. A. Brytov, and Yu. F. Sherpolov, USSR Acad. Sci. Bull. Phys. **28**, 1774 (1964).

[27]A. van Wijngaarden, J. Kwela, and G. W. F. Drake, in *Twelfth International Conference on Atomic Physics: Abstracts of Contributed Papers,* edited by W. E. Baylis, G. W. F. Drake, and J. W. McConkey (Publisher, Ann Arbor, MI,

1990), p. I-33.

[28]M. Narasimham and R. Strombotne, Phys. Rev. A **4**, 14 (1971).

[29]E. Lipworth and R. Novick, Phys. Rev. **108**, 1434 (1957).

[30]J. R. Sapirstein and D. R. Yennie, in *Quantum Electrodynamics,* edited by T. Kinoshita (World Scientific, Singapore, 1990). Our definition of the constants A_{ij}, $G(Z\alpha)$, etc. is smaller by a factor of $\frac{3}{4}$ in agreement with Refs. 5 and 32.

[31]W. R. Johnson and G. Soff, At. Data. Nucl. Data Tables **33**, 405 (1985).

[32]G. W. Erickson and D. R. Yennie, Ann. Phys. (N.Y.) **35**, 271 (1965).

[33]H. Grotch and D. R. Yennie, Rev. Mod. Phys. **41**, 350 (1969).

[34]M. A. Doncheski, H. Grotch, and G. W. Erickson, Phys. Rev. A **43**, 2152 (1991); M. A. Doncheski, H. Grotch, and D. A. Owen, *ibid.* **41**, 2851 (1990); G. W. Erickson and H. Grotch, Phys. Rev. Lett. **60**, 2611 (1988).

[35]D. J. Drickey and L. N. Hand, Phys. Rev. Lett. **9**, 521 (1962); L. N. Hand, D. J. Miller, and R. Wilson, Rev. Mod. Phys. **35**, 335 (1963).

[36]G. G. Simon, Ch. Schmidt, F. Borkowski, and V. H. Walther, Nucl. Phys. A **333**, 381 (1980).

[37]R. F. Frosch, J. S. McCarthy, R. E. Rand, and M. R. Yearian, Phys. Rev. **160**, 1308 (1966); R. F. Frosch, R. E. Rand, K. J. van Oostrum, and M. R. Yearian, Phys. Lett. **21**, 598 (1966).

[38]U. Erich, H. Frank, D. Haas, and H. Prange, Z. Phys. **208**, 209 (1968).

[39]I. Sick, J. S. McCarthy, and R. R. Whitney, Phys. Lett. **64B**, 33 (1976).

[40]E. Borie and G. A. Rinker, Phys. Rev. A **18**, 324 (1978).

[41]J. S. Cohen, Phys. Rev. A **25**, 1791 (1982).

[42]H. P. Von Arb, F. Dittus, H. Heeb, H. Hofer, F. Kottmann, S. Niggli, R. Schairen, D. Taqqu, J. Unternährer, and P. Egelhof, Phys. Lett. **136B**, 232 (1984).

[43]M. Eckhause, P. Guss, D. Joyce, J. R. Kane, R. T. Siegel, W. Vulcan, R. E. Welsh, R. Whyley, R. Dietlicher, and A. Zehnder, Phys. Rev. A **33**, 1743 (1986).

[44]L. Bracci and E. Zavattini, Phys. Rev. A **41**, 2352 (1990).

[45]A possible objection to the use of the muonic value for $r_{\rm rms}$ to determine the electronic Lamb shift is that the muonic Lamb shift must be known to deduce $r_{\rm rms}$ from the transition frequency, resulting in a circular argument. However the muonic Lamb shift is dominated by (electron) vacuum polarization, which is well known in comparison with the self-energy (see Refs. 46 and 47). In effect, vacuum polarization in the muonic system is being used to determine the electronic self-energy.

[46]G. W. F. Drake and L. L. Byer, Phys. Rev. A **32**, 713 (1985).

[47]R. Swainson and G. W. F. Drake, *ibid.* **34**, 620 (1986).

[48]P. J. Mohr, Ann. Phys. (N.Y.) **88**, 52 (1974) and Ref. 8.

[49]The recoil uncertainty of ± 0.6 MHz used in Ref. 30 should be reduced by a factor of 4 for $^4He^+$ to account for the $1/M$ scaling of this term.

[50]M. Leventhal, Phys. Rev. A **11**, 427 (1975).

[51]B. Curnutte, C. L. Cocke, and R. D. DuBois, Nucl. Instrum. Methods **202**, 119 (1981).

[52]G. P. Lawrence, C. Y. Fan, and S. Bashkin, Phys. Rev. Lett. **28**, 1612 (1972).

[53]M. Leventhal, D. E. Murnick, and H. W. Kugel, Phys. Rev. Lett. **28**, 1609 (1972).

[54]H. W. Kugel, M. Leventhal, D. E. Murnick, C. K. N. Patel, and O. R. Wood II, Phys. Rev. Lett. **35**, 647 (1975).

[55]J. Gassen, D. Müller, D. Budelski, L. Kremer, H.-J. Pross, F. Scheuer, P. von Brentano, A. Pape, and J. C. Sens, Phys. Lett. A **147**, 385 (1990).

[56]A. P. Georgiadis, D. Müller, H. D. Sträter, J. Gassen, P. von Brentano, J. C. Sens, and A. Pape, Phys. Lett. A **115**, 108 (1986).

[57]O. R. Wood II, C. K. N. Patel, D. E. Murnick, E. T. Nelson, M. Leventhal, H. W. Kugel, and Y. Niv, Phys. Rev. Lett. **48**, 398 (1982).

[58]H. Gould and R. Marrus, Phys. Rev. A **28**, 2001 (1983).

[59]C. T. Munger and H. Gould, Phys. Rev. Lett. **57**, 2927 (1986).

[60]Yu. L. Sokolov and V. P. Yakovlev, Zh. Eksp. Teor. Fiz. **83**, 15 (1982) [Sov. Phys.—JETP **56**, 7 (1982)]; V. G. Palchikov, Yu. L. Sokolov, and V. P. Yakovlev, Lett. J. Tech. Phys. **38**, 347 (1983).

[61]W. H. Press, B. P. Flannery, S. A. Teukolsky, and W. T. Vetterling, *Numerical Recipes* (Cambridge University Press, Cambridge, 1986), pp. 509-512.

[62]P. J. Mohr, At. Data. Nucl. Data Tables **29**, 453 (1983).